The Resistance of Clamped Sandwich Beams to Shock Loading

N. A. Fleck[1]

e-mail: naf1@eng.cam.ac.uk

V. S. Deshpande

Engineering Department,
Cambridge University,
Trumpington Street,
Cambridge, CB2 1PZ, UK

A systematic design procedure has been developed for analyzing the blast resistance of clamped sandwich beams. The structural response of the sandwich beam is split into three sequential steps: stage I is the one-dimensional fluid-structure interaction problem during the blast loading event, and results in a uniform velocity of the outer face sheet; during stage II the core crushes and the velocities of the faces and core become equalized by momentum sharing; stage III is the retardation phase over which the beam is brought to rest by plastic bending and stretching. The third-stage analytical procedure is used to obtain the dynamic response of a clamped sandwich beam to an imposed impulse. Performance charts for a wide range of sandwich core topologies are constructed for both air and water blast, with the monolithic beam taken as the reference case. These performance charts are used to determine the optimal geometry to maximize blast resistance for a given mass of sandwich beam. For the case of water blast, an order of magnitude improvement in blast resistance is achieved by employing sandwich construction, with the diamond-celled core providing the best blast performance. However, in air blast, sandwich construction gives only a moderate gain in blast resistance compared to monolithic construction. [DOI: 10.1115/1.1629109]

1 Introduction

A major consideration in the design of military vehicles (such as ships and aircraft) is their resistance to air and water blast. Early work (at the time of World War II) focused on monolithic plates, and involved measurement of blast resistance by full scale testing for a limited range of materials and geometries. Simple analytical models were also developed, such as the one-dimensional fluid-structure interaction model of Taylor [1].

Over the last decade a number of new core topologies for sandwich panels have emerged, showing structural advantage over monolithic construction for quasi-static loadings. These include metallic foams, [2], lattice materials of pyramidal and tetrahedral arrangement, [3], woven material, [4], and egg-box, [5]. The current study is an attempt to extend and to synthesize analytical models for the dynamic response of clamped beams in order to optimize the blast resistance of clamped sandwich beams. Explicit comparisons are made between the performance of competing core concepts.

The clamped sandwich beams, as sketched in Fig. 1, is representative of that used in the design of commercial and military vehicles: For example, the outermost structure on a ship comprizes plates welded to an array of stiffeners. While it is appreciated that the precise dynamic response of plates is different from that explored here for beams, the qualitative details will be similar, and major simplifications arise from the fact that simple analytical formulas can be derived for the beam.

In a parallel study, Xue and Hutchinson [6] have compared the blast resistance of clamped sandwich beams to that of monolithic beams of the same mass via three-dimensional finite element (FE) simulations. In these FE calculations, Xue and Hutchinson [6]

modeled the core topologies explicitly but ignored the fluid-structure interaction; a prescribed impulse was applied to the outer face of the sandwich beam and was applied uniformly to the monolithic beam. A limited number of FE calculations were performed to identify near-optimal sandwich configurations, and the superior blast resistance of sandwich beams compared to that of monolithic beams was demonstrated.

Review of the Characteristics of a Water Blast. The main characteristics of a shock wave resulting from an underwater explosion are well established due to a combination of detailed large-scale experiments and modeling over the past 60 years. Useful summaries of the main phenomena are provided by Cole [7] and Swisdak [8], and are repeated briefly here in order to underpin the current study.

The underwater detonation of a high explosive charge converts the solid explosive material into gaseous reaction products (on a time scale, t, of microseconds). The reaction products are at an enormous pressure (on the order of GPa), and this pressure is transmitted to the surrounding water by the propagation of a spherical shock wave at approximately sonic speed. Consider the response of a representative fluid element at a radial distance r from the explosion. Upon arrival of the primary shock wave, the pressure rises to a peak value p_o almost instantaneously. Subsequently, the pressure decreases at a nearly exponential rate, with a time constant θ on the order of milliseconds, and is given by $p(t) = p_o \exp(-t/\theta)$. The magnitude of the shock wave peak pressure and decay constant depend upon the mass and type of explosive material and the distance r. After the primary shock wave has passed, subsequent secondary shocks are experienced, due to the damped oscillation of the gas bubble which contains the explosive reaction products. However, these secondary shock waves have much smaller peak pressures, and are usually much less damaging than the primary shock to a structure in the vicinity of the explosion than the primary shock.

Experimental data (and physical models) support the use of simple power-law scaling relations between the mass m of explosive, the separation r between explosion and point of observation,
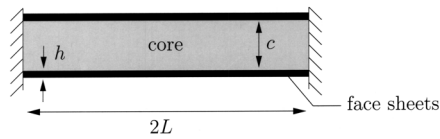
Fig. 1 Geometry of the sandwich beam

and the resulting shock wave characteristics, p_o and θ. For example, for an underwater TNT explosion, the peak pressure is taken from Table 2 of Swisdak [8] as

$$p_o = 52.4 \left(\frac{m^{1/3}}{r} \right)^{1.13} \qquad \text{MPa}, \qquad (1)$$

where m is in kilograms and r is in meters. Also, the time constant θ is

$$\theta = 0.084 m^{1/3} \left(\frac{m^{1/3}}{r} \right)^{-0.23} \qquad \text{ms}. \qquad (2)$$

These relations have been validated for the domain of m and r such that p_o lies in the range 3–140 MPa, see Swisdak [8] for further details. Similar scaling relations have been obtained for other high explosives, and the coefficients in the above relations hold to reasonable accuracy for them also.

Next consider the case of a blast wave in air due to the detonation of a high explosive. Again, a primary shock wave travels at near sonic speed, with an exponential pressure-time history at any fixed location from the explosive. The time constant for the pulse θ is similar in magnitude to that in water, but the peak pressure is an order of magnitude lower (see Ashby et al. [2] for a recent discussion, building upon the work of Smith and Hetherington [9]).

Scope and Motivation of the Study. The main objective of this study is to develop analytical formulas for characterizing the structural response of a sandwich beam subjected to blast loading in water or in air. These formulas are of direct practical use for designing laboratory-scale and industrial-scale blast-resistant sandwich beams, including the choice of face sheet and core.

First, the relevant mechanical response of candidate core topologies is reviewed. Second, the dynamic structural response of a clamped sandwich beam is analyzed; it is argued that the response can be separated into three distinct stages. Stage I is the response of the front face sheet to the primary shock wave, including the effects of fluid-structure interaction. Crushing of the core occurs in stage II. And in stage III the sandwich beam is brought to rest by plastic bending and stretching. Third, performance charts for a wide range of sandwich core topologies are constructed for both air and water blast, with the monolithic beam taken as the reference case. These performance charts are used to determine the optimal geometry to maximize blast resistance for a given mass of sandwich beam.

2 Review of Core Topologies

In recent years a number of micro-architectured materials have been developed for use as the cores of sandwich beams and panels. Here we briefly review the properties of the following candidate cores for application in blast-resistant construction: pyramidal cores, diamond-celled lattice materials, metal foams, hexagonal-honeycombs and square-honeycombs.

Pyramidal cores, as shown schematically in Fig. 2(a), are fabricated from sheet-metal by punching a square pattern and then by alternately folding the sheet to produce a corrugated pattern. The core is then bonded to the solid faces by brazing. The pyramidal core has an out-of-plane effective modulus (and longitudinal shear modulus) which scale linearly with the relative density $\bar{\rho}$ of the core. Provided the struts are sufficiently stocky for the elastic
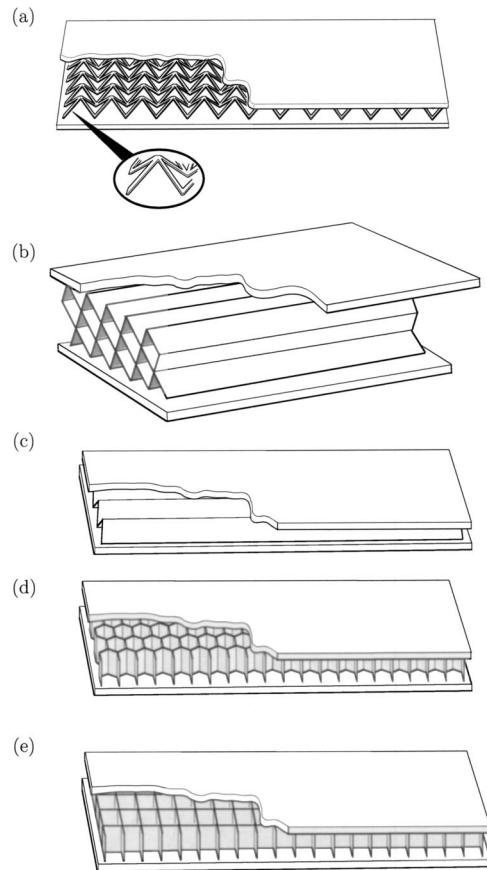

Fig. 2 Sketches of the sandwich core topologies; (a) pyramidal core, (b) diamond-celled core, (c) corrugated core, (d) hexagonal-honeycomb core, and (e) square-honeycomb core

buckling strength of the struts to exceed their yield strength, the out-of-plane compressive strength of the pyramidal core also scales linearly with $\bar{\rho}$. A detailed discussion on the mechanical properties of lattice materials such as pyramidal cores has been given previously by Deshpande and Fleck [3]. For example, the normal compressive strength σ_{nY} of the pyramidal core with the struts making an angle $\omega = 45°$ with the face sheets is

$$\frac{\sigma_{nY}}{\sigma_Y} = \begin{cases} 0.5\bar{\rho} & \text{set by yield, if } \bar{\rho} > \dfrac{96\sqrt{2}\,\epsilon_Y}{\pi^2} \\ \dfrac{\pi^2}{96\sqrt{2}\,\epsilon_Y}\bar{\rho}^2, & \text{set by elastic buckling, otherwise,} \end{cases} \qquad (3)$$

where σ_Y and ϵ_Y are the uniaxial yield strength and strain of the solid material from which the pyramidal core is made. Here we have assumed that the core struts are pin-jointed to the face sheets in order to get a conservative estimate of the elastic buckling strength. The in-plane strength of the pyramidal core in the length direction of the sandwich beam is governed by the bending strength of the nodes. Consequently, the in-plane strength scales as $\bar{\rho}^{3/2}$ and at the low relative densities for which these pyramidal cores find application, this strength is negligible, $\sigma_{lY} = 0$.

Diamond-celled lattice materials have the geometry shown in Fig. 2(b), and have recently been proposed as cores of sandwich beams. These lattice materials can be manufactured either by brazing together wire meshes, [4], or slotting together sheet metal. With the diamond-like cells aligned along the longitudinal axis of the beam as shown in Fig. 2(b), these materials provide high

strengths in both the normal and longitudinal directions of the beam. Typically diamond-cells have a semi-angle $\omega = 45°$ and the core has a normal compressive strength

$$\frac{\sigma_{nY}}{\sigma_Y} = \begin{cases} 0.5\bar{\rho}, & \text{set by yield, if } \bar{\rho} > \dfrac{4\sqrt{3}\epsilon_Y}{\pi}; \\[2ex] \dfrac{\pi^2}{96\epsilon_Y}\bar{\rho}^3, & \text{set by elastic buckling, otherwise,} \end{cases}$$

(4a)

while the longitudinal strength is given by

$$\frac{\sigma_{lY}}{\sigma_Y} = \bar{\rho}.$$

(4b)

Note that the diamond-celled core has identical strength-density relations to the single layered corrugated core shown in Fig. 2(c). However, unlike in a corrugated core, the size of the diamond-cells can be varied independently from the sandwich beam core thickness and hence made as small as required to prevent wrinkling of the sandwich face sheets.

Metal foams are random cellular solids with a highly imperfect microstructure. In most cases they are close to isotropic in elasto-plastic properties. The connectivity of neighboring cell edges is sufficiently small for the cell walls to bend under all macroscopic stress states, Ashby et al. [2]. Consequently, the modulus scales quadratically with relative density $\bar{\rho}$, while the macroscopic yield strength scales with $\bar{\rho}^{3/2}$ according to, [2],

$$\frac{\sigma_{nY}}{\sigma_Y} = \frac{\sigma_{lY}}{\sigma_Y} = 0.3\bar{\rho}^{3/2}.$$

(5)

Hexagonal-honeycombs are extensively used as cores of sandwich beams in the configuration sketched in Fig. 2(d), i.e., with the out-of-plane direction of the honeycomb aligned along the transverse direction of the beam. Thus, neglecting the elastic buckling of the cell walls we take

$$\frac{\sigma_{nY}}{\sigma_Y} = \bar{\rho}.$$

(6)

On the other hand, in the longitudinal direction of the beam, hexagonal-honeycomb cores deform by the formation of plastic hinges at the nodes which results in a negligible strength. Thus, in practical applications it is reasonable to assume $\sigma_{lY} = 0$ for these honeycombs.

Square-honeycombs as sketched in Fig. 2(e) can be manufactured by slotting together sheet metal. With the square cells aligned parallel to the longitudinal axis of the beam as sketched in Fig. 2(e), the square-honeycomb core provides high strength in both the normal and longitudinal directions. Neglecting elastic buckling of the cell walls in the normal direction, the normal and longitudinal strength of the square-honeycomb are given by

$$\frac{\sigma_{nY}}{\sigma_Y} = \bar{\rho}, \quad \text{and,}$$

(7a)

$$\frac{\sigma_{lY}}{\sigma_Y} = 0.5\bar{\rho},$$

(7b)

respectively.

All the cores discussed above have their relative advantages and disadvantages with regards to properties, ease of manufacture and cost. For the purposes of judging the relative performance of the cores described above we define an "ideal" core. The "ideal" core has optimal strengths in the normal and longitudinal directions given by

$$\frac{\sigma_{nY}}{\sigma_Y} = \frac{\sigma_{lY}}{\sigma_Y} = \bar{\rho}.$$

(8)

This core is 100% efficient in carrying load in both these directions. It is not clear whether such a core is physically realizable: The diamond-celled core with the diamond cells aligned along the longitudinal axis of the beam or a square-honeycomb come closest to this "ideal" performance.

3 Analytical Models for the Structural Response of a Clamped Sandwich Beam to Blast Loading

For the sandwich beam, the structural response is split into a sequence of three stages: stage I is the one-dimensional fluid-structure interaction problem during the blast event, and results in a uniform velocity being imposed on the outer face sheet; stage II is the phase of core crush, during which the velocities of the faces and core equalize by momentum transfer; stage III is the retardation phase during which the beam is brought to rest by plastic bending and stretching. This analysis is used to calculate the transverse displacement (and longitudinal tensile strain accumulated) of selected sandwich beams as a function of the magnitude of blast loading.

3.1 Order-of-Magnitude Estimate for the Time Scale of Each Stage of the Dynamic Response. The justification for splitting the analysis into three distinct stages is the observation that the time periods for the three phases differ significantly. The duration of the primary shock for a typical blast wave in air or water due to the detonation of an explosive is of the order of 0.1 ms. In contrast, the period for core crush is approximately 0.4 ms, argued as follows. Suppose that a blast wave in water provides an impulse of 10^4 Nsm^{-2} to a steel sandwich structure, with a 10 mm thick face sheet. Then, the front face acquires an initial velocity v_o of 127 ms^{-1}. On taking the core to have a thickness of $c = 100$ mm and a densification strain $\epsilon_D = 0.5$, the compression phase lasts for $\epsilon_D c / v_o = 0.39$ ms. In contrast, the structural response time is on the order of 25 ms: this can be demonstrated by considering the dynamic response of a stretched rigid-ideally plastic string. Consider a string of length $2L$, gripped at each end, made from a material of density ρ_f and uniaxial yield strength σ_{fY}. Then, the transverse equation of motion for the membrane state is

$$\rho_f \ddot{w} - \sigma_{fY} \frac{\partial^2 w}{\partial x^2} = 0,$$

(9)

where $w(x,t)$ is the transverse displacement, the overdot denotes differentiation with respect to time t, and x is the axial coordinate from one end of the string. For illustrative purposes, assume the string is given an initial velocity profile $\dot{w}(t=0) = \dot{w}_o \sin(\pi x / 2L)$. Then, the solution of (9) is

$$w = \frac{2\dot{w}_o L}{\pi} \sqrt{\frac{\rho_f}{\sigma_{fY}}} \sin\left(\frac{\pi}{2L}\sqrt{\frac{\sigma_{fY}}{\rho_f}}t\right) \sin\frac{\pi x}{2L}.$$

(10)

The string attains its maximum displacement and comes to rest after a time

$$T = L\sqrt{\frac{\rho_f}{\sigma_{fY}}}.$$

(11)

Now substitute representative values for the case of a steel ship hull: $L = 5$ m, $\rho_f = 7850$ kgm^{-3}, and $\sigma_{fY} = 300$ MPa, gives $T = 25$ ms, as used above.

3.2 Stage I: One-Dimensional Fluid-Structure Interaction Model. Consider the simplified but conservative idealisation of a plane wave impinging normally and uniformly upon an infinite sandwich plate. For most practical geometries and blast events, the time scale of the blast is sufficiently brief for the front face of a sandwich panel to behave as a rigid plate of mass per unit area m_f. We adopt the one-dimensional analysis of Taylor [1], and consider an incoming wave in the fluid of density ρ_w, traveling with a constant velocity c_w in the direction of increasing x mea-

sured perpendicular to the sandwich panel. The origin is taken at the front face of the sandwich panel, and the transverse deflection of the face is written as $w(t)$ in terms of time, t. Then, the pressure profile for the incoming wave can be taken as

$$p_I(x,t) = p_o e^{-(t-x/c_w)/\theta}, \tag{12}$$

upon making the usual assumption of a blast wave of exponential shape and time constant θ (on the order of 0.1 ms, as discussed above). The magnitude of the peak pressure p_o is typically in the range 10–100 MPa, and far exceeds the static collapse pressure for the sandwich plate (typically on the order of 1 MPa).

If the front face were rigid and fixed in space, the reflected wave would read

$$p_{r1}(x,t) = p_o e^{-(t+x/c_w)/\theta}, \tag{13}$$

corresponding to perfect reflection of the wave, traveling in the $-x$ direction. But the front face sheet is not fixed: it accelerates as a rigid body with a mass per unit area m_f, and moves with a velocity $\dot{w}(t)$. Consequently, the fluid elements adjacent to the front face possess the common velocity $\dot{w}(t)$, and a rarefaction wave p_{r2}, of magnitude

$$p_{r2}(x,t) = -\rho_w c_w \dot{w}\left(t + \frac{x}{c_w}\right), \tag{14}$$

is radiated from the front face. Thus, the net water pressure $p(x,t)$ due to the incoming and reflected waves is

$$p(x,t) = p_I + p_{r1} + p_{r2} = p_o\left[e^{-(t-x/c_w)/\theta} + e^{-(t+x/c_w)/\theta}\right]$$
$$- \rho_w c_w \dot{w}\left(t + \frac{x}{c_w}\right). \tag{15}$$

The front face of the sandwich panel (at $x=0$) is accelerated by the net pressure acting on it, giving the governing ordinary differential equation for face motion as

$$m_f \ddot{w} + \rho_w c_w \dot{w} = 2 p_o e^{-t/\theta}. \tag{16}$$

Upon imposing the initial conditions $w(0) = \dot{w}(0) = 0$, and defining the nondimensional measure $\psi \equiv \rho_w c_w \theta / m_f$, the solution of (16) is

$$w(t) = \frac{2 p_o \theta^2}{m_f(\psi-1)\psi}[(\psi-1) + e^{-\psi t/\theta} - \psi e^{-t/\theta}], \tag{17}$$

and the pressure distribution follows immediately via (15). In particular, the pressure on the front face is

$$p(t,x=0) = 2 p_o e^{-t/\theta} - \frac{2 p_o \psi}{\psi-1}[e^{-t/\theta} - e^{-\psi t/\theta}]. \tag{18}$$

For the case of a liquid containing dissolved gases, the pressure loading on the front face ceases and the liquid cavitates when $p(t,x=0) \to 0$, thereby defining the cavitation time τ_c. Substitution of this condition into (18) provides the simple relation

$$\frac{\tau_c}{\theta} = \frac{1}{\psi-1} \ln \psi, \tag{19}$$

and the impulse conveyed to the face follows from (17) as

$$I_{\text{trans}} = \zeta I \tag{20a}$$

where

$$\zeta \equiv \psi^{-\psi/\psi-1}, \tag{20b}$$

and I is the maximum achievable impulse given by

$$I = \int_0^{\infty} 2 p_o e^{-t/\theta} dt = 2 p_o \theta. \tag{21}$$

This maximum impulse is only realized for the case of a stationary rigid front face. The ratio I_{trans}/I is plotted as a function of the fluid-structure interaction parameter ψ in Fig. 3; the transmitted
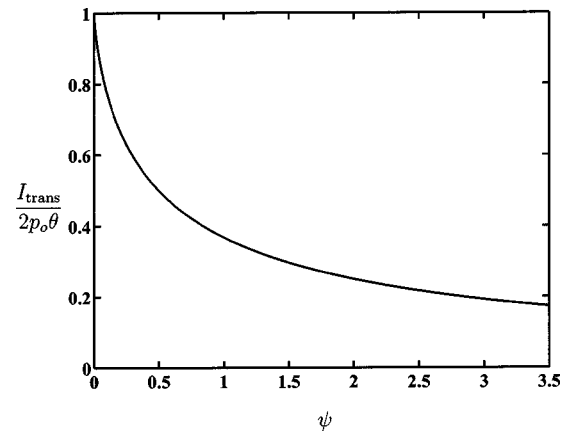

Fig. 3 The ratio of the impulse transmitted to the structure I_{trans}, and the impulse transmitted to a fixed rigid structure $2p_o\theta$, as a function of the fluid-structure interaction parameter ψ

impulse decreases substantially with increasing ψ. It is instructive to substitute some typical values for air and water blast into relations (19) and (20b) in order to assess the knock down in transmitted impulse and the magnitude of the cavitation time in relation to the blast time constant θ due to the fluid-structure interaction. For the case of an air blast, we take $\rho_w = 1.24$ kgm^{-3}, $c_w = 330$ ms^{-1}, $\theta = 0.1$ ms, and $m_f = 78$ kgm^{-2} for a 10 mm thick steel plate. Hence, we find that $\psi = 0.052$, $\tau_c/\theta = 3.1$ and $I_{\text{trans}}/I \approx 0.85$. In contrast, a water blast, we take $\rho_w = 1000$ kgm^{-3}, $c_w = 1400$ ms^{-1}, $\theta = 0.1$ ms, $m_f = 78$ kgm^{-2}; this implies the values $\psi = 1.79$, $\tau_c/\theta = 0.74$ and $I_{\text{trans}}/I = 0.267$. We conclude that a significant reduction in transferred impulse can be achieved by employing a light face sheet for the case of water blast, while for air blast the large jump in acoustic impedance between air and the solid face sheet implies that all practical designs of solid face sheet behave essentially as a fixed, rigid face with full transmission of the blast impulse. We anticipate that sandwich panels with light faces can be designed to ensure the reduced transmission of impulse from an incoming water blast wave.

In summary, the first phase of the analysis comprises the acceleration of the front face to a velocity v_o by the incoming (and reflected) primary shock wave. The core and back face of the sandwich beam remain stationary during this initial stage. It is instructive to obtain order of magnitude estimates for the initial velocity of the front face, and its deflection at time $t = \tau_c$. For an impulse of magnitude 10^3 Nsm^{-2} in air, and 10^4 Nsm^{-2} in water, the acquired velocity of the front face is approximately 13 ms^{-1} for the air blast, and 34 ms^{-1} for the water blast (steel face sheet, of thickness 10mm). Relation (17) reveals that the lateral deflection of the front face is 2.5 mm for the air blast and 1.83 mm for the water blast. It is expected that sandwich beams for ship application will be of core thickness c of order 0.1–1.0 m, and so the degree of core compression during the initial phase of blast loading is negligible.

Taylor [1] has modeled the influence of structural support to the dynamic response of the face sheet by adding the term kw to (16), corresponding to a uniformly distributed restraining force of magnitude kw giving

$$m_f \ddot{w} + \rho_w c_w \dot{w} + kw = 2 p_o e^{-t/\theta}. \tag{22}$$

The physical interpretation is that k denotes the structural stiffness due to an array of supports between the face sheet and the underlying, motionless structure. By solving (22), and considering representative values for k for the case of a steel plate on a ship

superstructure, Taylor demonstrated that the stiffness term can be neglected with little attendant loss of accuracy. The main objective of the current study is to compare the relative performance of various sandwich panel configurations, and so the simplified analysis is adequate for our purposes.

3.3 Stage II: One-Dimensional Model of Core Compression Phase.

In the second phase of motion it is envisaged that the core is crushed by the advancing outer face sheet, and consequently the outer face sheet is decelerated by the core while the core and the rear face of the sandwich beam are accelerated. For simplicity, we consider a one-dimensional slice through the thickness of the sandwich beam and neglect the reduction in momentum due to the impulse provided by the supports. This approximation is motivated by noting that the time period of this phase is much smaller than the overall structural response time of the structure. Subsequent retardation of the sandwich beam is due to plastic bending and stretching in Stage III of the motion. Detailed finite element calculations carried out recently by Qiu et al. [10] support this assertion. The core is treated as a rigid, ideally plastic crushable solid with a nominal crush strength σ_{nY} up to a nominal densification strain ϵ_D. After densification has been achieved, it is assumed that the core is rigid.

Overall considerations of energy and momentum conservation can be used to determine the final value of core compressive strain $\epsilon_c (\leqslant \epsilon_D)$ and the final common velocity v_f of faces and core at the end of the core crush stage. The quantities ϵ_c and v_f suffice to proceed with the third stage of analysis to calculate the beam deflection. However, if additional information on the core crush phase is to be obtained, such as the time for core crush T_c, a one-dimensional plastic shock wave analysis is required. First, we present the immediate results for ϵ_c and v_f, and then we outline the shock wave analysis in order to obtain T_c.

Momentum conservation during core crush dictates that

$$(2m_f + \rho_c c)v_f = m_f v_o, \tag{23}$$

and so a direct relation exists between the common velocity of the sandwich beam v_f after core crush and the initial velocity of the outer face, v_o. The ratio of the energy lost U_{lost} in this phase to the initial kinetic energy of the outer face sheet is then given by

$$\frac{U_{\text{lost}}}{m_f v_o^2 / 2} = \frac{1 + \hat{\rho}}{2 + \hat{\rho}} \tag{24}$$

where $\hat{\rho} = \rho_c c / m_f$. This loss in energy is dissipated by plastic dissipation in compressing the core and thus we equate

$$U_{\text{lost}} = \sigma_{nY} \epsilon_c c, \tag{25}$$

where ϵ_c is the average compressive strain in the core. Combining the two above relation, the core compression strain ϵ_c is given by

$$\epsilon_c = \frac{\epsilon_D}{2} \frac{\hat{\rho} + 1}{\hat{\rho} + 2} \hat{I}^2, \tag{26}$$

in terms of the dimensionless parameter $\hat{I} = I_{\text{trans}} / \sqrt{m_f c \sigma_{nY} \epsilon_D}$. However, if U_{lost} is too high such that ϵ_c as given by (26) exceeds the densification strain ϵ_D, then ϵ_c is set to the value ϵ_D and additional dissipation mechanisms must occur for energy conservation. The above analysis neglects any such additional mechanisms. FE calculations by Xue and Hutchinson [6] and Qiu et al. [10] reveal that the additional mechanism are tensile stretching of the outer face near the supports together with additional crushing of the core under sharply increasing stress.

Now a word of warning. The Stage II analysis neglects the impulse provided by the support reactions during the core compression phase. This assumption breaks down for stubby beams subjected to large impulses; the quality of the approximation is analyzed in detail by Qiu et al. [10] via a set of dynamic finite element calculations.
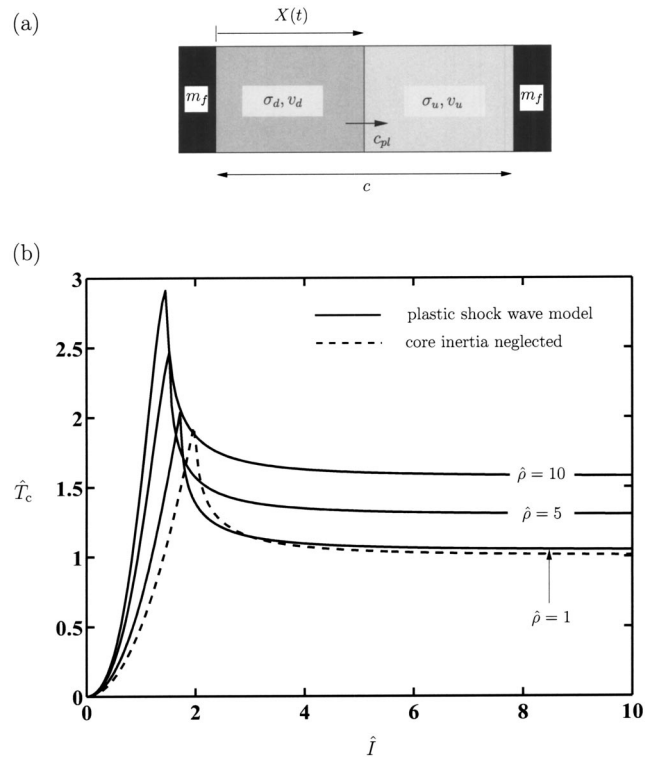
Fig. 4 (*a*) **Sketch of the propagation of a one-dimensional shock in the sandwich core,** (*b*) **the nondimensional core compression time** $\hat{T}_c$ **as a function of the nondimensional impulse** $\hat{I}$ **transmitted to the structure**

Plastic Shock-Wave Analysis. The above analysis assumes that the core compresses uniformly through its thickness at constant stress. In reality, the core can compress nonuniformly due to buckling of strut elements within the core and due to inertial effects. Here, we consider the case of a core which contains a sufficiently large number of microstructural units (the cells of a metal foam, or the units of a diamond-celled core) for it to be represented by a porous solid. However, the role of inertia is included, and a plastic shock wave analysis is performed in order to deduce the spatial and temporal evolution of strain within the core.

Consider a sandwich structure, with face sheets of mass per unit area m_f, and a core of initial thickness c and relative density ρ_c. The front face sheet has an initial velocity v_o, while the core and inner face sheet are initially at rest. As assumed above, we consider a one-dimensional problem as sketched in Fig. 4(*a*) with the core treated as a rigid, ideally plastic solid with a nominal crush strength σ_{nY} up to a nominal densification strain ϵ_D; at densification the core locks up and becomes rigid. After impact of the front face sheet upon the core, a plastic shock wave moves through the core at a velocity c_{pl}. Suppose that the shock wave has advanced by a distance X after a time t has elapsed, as sketched in Fig. 4(*a*). Upstream of the shock wave, the undeformed core and rear face of sandwich beam have a velocity v_u, whilst downstream of the shock wave the core has compacted to the densification strain ϵ_D and shares the velocity v_d with the front face. The propagation behavior of the shock wave can be determined by numerical integration as follows.

Conservation of momentum dictates

$$[m_f + \rho_c(c - X)]v_u + [m_f + \rho_c X]v_d = m_f v_o, \tag{27}$$

while energy conservation states

$$\frac{1}{2}m_f v_o^2 = \frac{1}{2}[m_f + \rho_c(c-X)]v_u^2 + \frac{1}{2}[m_f + \rho_c X]v_d^2 + \sigma_{nY}\epsilon_D X,$$
(28)

and mass conservation across the shock wave provides

$$c_{pl}\epsilon_D = v_d - v_u.$$
(29)

Now the compressive stress on the upstream face of the shock wave is related directly to the mass and acceleration of upstream material, giving

$$\sigma_u = [m_f + \rho_c(c-X)]\dot{v}_u,$$
(30)

and a similar relation holds for the compressive stress on the downstream face of the shock wave,

$$\sigma_d = -[m_f + \rho_c X]\dot{v}_d.$$
(31)

Time differentiation of (27) and the elimination of $(\dot{v}_u, \dot{v}_d)$ from the resulting expression via (30) and (31) leads to the well-known statement of momentum conservation across the shock wave,

$$\sigma_u - \sigma_d = \rho_c c_{pl}(v_u - v_d).$$
(32)

As the shock wave progresses through the core it slows down, and, for a sufficiently low initial value of front face velocity v_o, the shock wave arrests at a travel X_c less than the core thickness c. Upon noting that $\dot{X} = c_{pl}$ the crush time T_c is calculated via (29) to give

$$T_c = \int_0^{X_c} \frac{dX}{c_{pl}} = \int_0^{X_c} \frac{\epsilon_D}{v_d - v_u} dX.$$
(33)

Now $(v_d - v_u)$ can be expressed as a function of X via (27) and (28), and (33) thereby integrated numerically in order to obtain the core crush time, T_c. The integral reads in nondimensional form,

$$\hat{T}_c = \frac{T_c v_o}{\epsilon_D c} = \int_0^{\bar{X}_c} \frac{1}{\bar{v}_d - \bar{v}_u} d\bar{X},$$
(34)

where $\bar{X} \equiv X/c$, $\bar{X}_c \equiv X_c/c = \epsilon_c/\epsilon_D$, as specified by (26), $\bar{v}_d \equiv v_d/v_o$ and $\bar{v}_u \equiv v_u/v_o$. In the above relation $\bar{v}_d - \bar{v}_u$ depends upon $\bar{X}$ according to

$$(\bar{v}_d - \bar{v}_u)^2 = \frac{1 + \hat{\rho}(2-\bar{X}) + \hat{\rho}^2(1-\bar{X})}{[1+\hat{\rho}(1-\bar{X})]^2(1+\hat{\rho}\bar{X})}$$

$$- \frac{2(2+\hat{\rho})\hat{\rho}\bar{X}}{[1+\hat{\rho}(1-\bar{X})](1+\hat{\rho}\bar{X})\hat{I}^2}.$$
(35)

For the case $\bar{X} \equiv X/c < 1$, $\hat{T}_c$ is calculated as a function of $\hat{I}$ by evaluating (34), with $(\bar{v}_d - \bar{v}_u)$ expressed by (35), and the upper limit of integration $\bar{X}_c = \epsilon_c/\epsilon_D$ expressed in terms of $\hat{I}$ via (26). However, at sufficiently high values of impulse $\hat{I}$, the plastic shock wave traverses the thickness of the core c without arrest. The period of core compression is again specified by (34), with $(\bar{v}_d - \bar{v}_u)$ expressed by (35), and the upper limit of integration $\bar{X}_c = 1$.[1] At the transition value $\hat{I}_t$, the shock wave arrests at the same instant that it traverses the core thickness; $\hat{I}_t$ is obtained by equating ϵ_c to ϵ_D in (26), to give

$$\hat{I}_t^2 = \frac{2(\hat{\rho}+2)}{\hat{\rho}+1}.$$
(36)

It is noted in passing that $\hat{I}_t$ is only mildly sensitive to the magnitude of the mass ratio $\hat{\rho}$: as $\hat{\rho}$ is increased from zero (negligible core mass) to infinity (negligible face sheet mass), $\hat{I}$ decreases

---

[1]Note that in such cases the above analysis conserves momentum but does not account for the additional dissipation mechanisms required to conserve energy.

from 2 to $\sqrt{2}$. Thus, it is predicted that the plastic shock wave will arrest before it traverses the core provided $\hat{I}$ is less than $\sqrt{2}$ for all ratios of core to face sheet mass.

The dependence of $\hat{T}_c = T_c v_o / \epsilon_D c$ on $\hat{I}$ is shown in Fig. 4(b) for selected values of $\hat{\rho}$. It is clear from the figure that $\hat{T}_c$ increases from zero to a peak value as $\hat{I}$ increases from zero to the transition value $\hat{I}_t$. At higher values of $\hat{I}$, $\hat{T}_c$ decreases: at very large values of $\hat{I}$, $\hat{T}_c$ approached a finite asymptote which equals unity for the case $\hat{\rho}=0$. It is assumed that the core becomes rigid after it has densified, and the core and face sheet velocities instantaneously jump in value to v_f at $\hat{T} = \hat{T}_c$.

Simple analytical expressions for the dependence of $\hat{T}_c$ upon $\hat{I}$ can be obtained in the limiting case of a negligible core mass, $\hat{\rho} \to 0$. Consider first the case where the impulse is sufficiently small for the core to compress by a strain ϵ_c less than the densification value ϵ_D. Then, the core provides a constant compression stress σ_{nY} upon the front and back face sheets, so that the front face has the velocity

$$v_d = v_o - \frac{\sigma_{nY}t}{m_f},$$
(37)

while the rear face has the velocity

$$v_u = \frac{\sigma_{nY}t}{m_f}.$$
(38)

The core compression time T_c is obtained by equating v_d and v_u, to obtain

$$\hat{T}_c = \frac{\hat{I}^2}{2}.$$
(39)

Continuing with the choice $\hat{\rho} \to 0$, now address the case where the impulse exceeds the transition value $\hat{I}_t = 2$, so that the core densifies before the front and rear-face sheet velocities have equalized to $v_o/2$, as demanded by momentum conservation. The core compression time is set by the time for the face sheets to undergo a relative approach of $\epsilon_D c$. Upon noting that the front face sheet displaces by

$$s_d = v_o t - \frac{\sigma_{nY}}{2m_f}t^2,$$
(40)

while the back face sheet displaces by

$$s_u = \frac{\sigma_{nY}}{2m_f}t^2,$$
(41)

the core compression time T_c is determined by the condition

$$s_d - s_u = v_o T_c - \frac{\sigma_{nY}}{m_f}T_c^2 = \epsilon_D c.$$
(42)

with solution

$$\hat{T}_c \equiv \frac{T_c v_o}{\epsilon_D c} = \frac{\hat{I}}{2}[\hat{I} - \sqrt{\hat{I}^2 - 4}].$$
(43)

3.4 Stage III: Dynamic Structural Response of Clamped Sandwich Beam. At the end of stage II the core and face sheets have a uniform velocity v_f as dictated by (23). The final stage of sandwich response comprises the dissipation of the kinetic energy acquired by the beam during stages I and II by a combination of beam bending and longitudinal stretching. The problem under consideration is a classical one: what is the dynamic response of a clamped beam of length $2L$ made from a rigid ideally-plastic material with mass per unit length m subjected to an initial uniform transverse velocity v_f? This problem has been investigated by a number of researchers. In particular, Symmonds [11] developed analytical solutions based on a small displacement analysis while Jones [12] developed an approximate method for large dis-
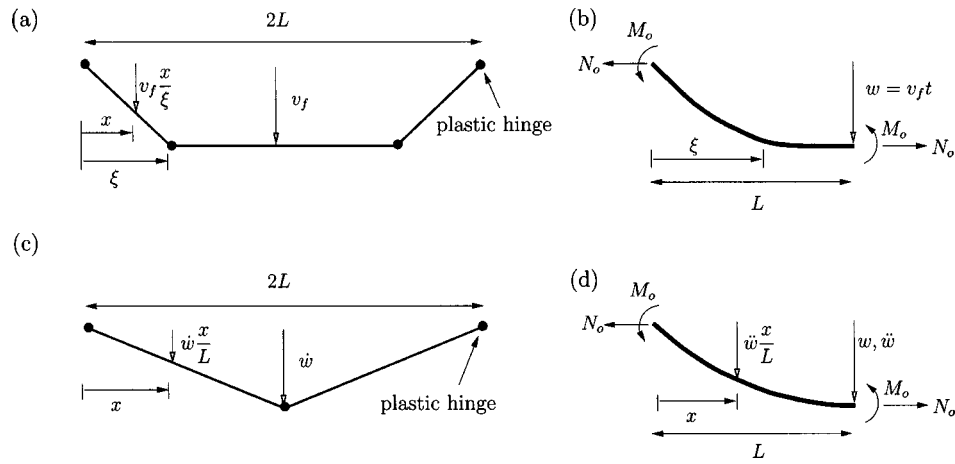
Fig. 5 Analysis of stage III of the blast response. (*a*) Velocity profile in phase I, (*b*) a free-body diagram of the half-beam in phase I, with the deflected shape sketched approximately, (*c*) velocity profile in phase II, and (*d*) a free-body diagram of the half-beam in phase II, with the deflected shape sketched approximately. The accelerations of the beam are shown in (*d*).

placements using an energy balance method. These methods are summarized in Jones [13]. Here we present an approximate solution that is valid in both the small and large displacement regime: it reduces to the exact small displacement solution of Symmonds [11] for small v_f and is nearly equal to the approximate large deflection solution of Jones [13] for large v_f.

Active plastic straining in the beam is by a combination of plastic bending and longitudinal stretching with shear yielding neglected: An evaluation of the magnitude of the transient shear force within the face sheet in the dynamic clamped beam calculation of Jones [13] reveals that shear yielding is expected only for unrealistic blast pressures as discussed above. We assume that yield of an beam element is described by the resultant longitudinal force N and the bending moment M. The shape of the yield surface in (N,M) space for a sandwich beam depends on the shape of the cross section and the relative strength and thickness of the faces and the core. A yield locus described by

$$\frac{|M|}{M_o}+\frac{|N|}{N_o}=1, \tag{44}$$

where N_o and M_o are the plastic values of the longitudinal force and bending moment, respectively, is highly accurate for a sandwich beam with thin, strong faces and a thick, weak core. It becomes less accurate as the beam section approached the monolithic limit. It is difficult to obtain a simple closed-form analytical solution for the dynamic beam response with this choice of yield surface. Here, we approximate this yield locus to be a circumscribing square such that

$$|N|=N_o \tag{45a}$$

$$|M|=M_o, \tag{45b}$$

with yield achieved when one or both of these relations are satisfied. We could equally well approximate the yield locus to be an inscribing square such that

$$|N|=0.5N_o \tag{46a}$$

$$|M|=0.5M_o, \tag{46b}$$

with again at yield one or both of these relations satisfied. Jones [13] has explored the choice of circumscribing and inscribing yield surfaces for a monolithic beam and shown that the resulting solutions bound the exact response. We proceed to develop the analysis for the circumscribing yield locus: the corresponding formulas for the inscribed locus may be obtained by replacing M_o by $0.5M_o$ and N_o by $0.5N_o$.

In the dynamic analysis we shall assume that displacements occur only in a direction transverse to the original axis of the beam and thus stretching is a result of only transverse displacements. Moderate transverse deflections are considered, such that the deflection w at the mid-span of the beam is assumed to be small compared to the beam length $2L$ and the longitudinal force $N=N_o$ can be assumed to be constant along the beam. The motion of the beam can be separated into two phases as in the small displacement analysis of Symmonds [11]. In phase I, the central portion of the beam translates at the initial velocity v_f while segments of length ξ at each end rotate about the supports. The bending moment is taken to vary from $-M_o$ at the outer stationary plastic hinges at the supports to $+M_o$ at ends of the segments of length ξ with the bending moment constant in the central flat portion. Thus, time increments in curvature occur only at the ends of the rotating segments while axial straining is distributed over the length of the rotating segments. A free-body diagram for half of the clamped beam is shown in Fig. 5(*b*); conservation of the moment of momentum about a fixed end after a time t gives

$$(mLv_f)\frac{L}{2}=m(L-\xi)v_f\left(\xi+\frac{L-\xi}{2}\right)+2M_ot+\frac{1}{2}N_ov_ft^2$$
$$+\int_0^\xi\frac{mv_fx^2}{\xi}dx, \tag{47}$$

where x is the axial coordinate from one end of the beam, as shown in Fig. 5(*b*). This equation gives ξ as a function of time t

$$\xi=\sqrt{\frac{3t(v_fN_ot+4M_o)}{mv_f}}. \tag{48}$$

Phase I continues until the traveling hinges at the inner ends of the segments of length ξ coalesce at the midspan, i.e., $\xi=L$. Thus, from (48), phase I ends at a time T_1

$$T_1=\frac{M_o}{N_ov_f}\left[\sqrt{4+\frac{mL^2v_f^2N_o}{3M_o^2}}-2\right], \tag{49}$$

and the displacement of the mid-span w_1 at this time is given by

$$w_1=v_fT_1=\frac{M_o}{N_o}\left[\sqrt{4+\frac{mL^2v_f^2N_o}{3M_o^2}}-2\right]. \tag{50}$$

In phase II of the motion, stationary plastic hinges exist at the midspan and at the ends of the beam, with the moment varying between $-M_o$ at the beam end to $+M_o$ at the midspan. The

velocity profile is triangular, as sketched in Fig. 5(c). The equation of motion of the half-beam in phase II follows from the free-body diagram sketched in Fig. 5(d) as

$$2M_o + N_o w = -\frac{\ddot{w}}{L}\int_0^L m x^2 dx = -\frac{mL^2}{3}\ddot{w}, \qquad (51)$$

where x is the axial coordinate from one end of the beam as shown in Fig. 5(d). With initial conditions $w(T_1) = w_1$ and $\dot{w}(T_1) = v_f$, this differential equation admits a solution of the form

$$w(t) = \frac{v_f}{\omega}\sin[\omega(t - T_1)] + \left(\frac{2M_o}{N_o} + w_1\right)\cos[\omega(t - T_1)] - \frac{2M_o}{N_o}, \qquad (52a)$$

where

$$\omega = \frac{1}{L}\sqrt{\frac{3N_o}{m}}. \qquad (52b)$$

The maximum deflection w of the midspan of the beam occurs at a time T when $\dot{w}(T) = 0$. Upon substituting this termination condition in the velocity equation, as given by the time derivative of (52a), the response time T is obtained as

$$T = T_1 + \frac{1}{\omega}\tan^{-1}\left[\frac{N_o v_f}{\omega(2M_o + w_1 N_o)}\right], \qquad (53)$$

and the corresponding maximum deflection of the midspan of the beam is

$$w = \sqrt{\frac{v_f^2}{\omega^2} + \left(\frac{2M_o}{N_o} + w_1\right)^2} - \frac{2M_o}{N_o}. \qquad (54)$$

The deflected shape of the beam can be obtained using the procedure detailed on p. 81 of Jones [13] but the derivation and result are omitted here as they are not central to the present discussion.

We specialize this analysis to the case of sandwich beams. Recall that we are considering clamped sandwich beams of span $2L$ with identical face sheets of thickness h and a core of thickness c, as shown in Fig. 1. The face sheets are made from a rigid ideally plastic material of yield strength σ_{fY} and density ρ_f, while the core of density ρ_c has a normal compressive strength σ_{nY} and a longitudinal strength σ_{lY}. The plastic bending moment of the sandwich beam with the compressed core is given by

$$M_o = \sigma_{lY}\frac{(1-\epsilon_c)c^2}{4} + \sigma_{fY}h[(1-\epsilon_c)c + h], \qquad (55)$$

while the plastic membrane force N_o is given by

$$N_o = 2\sigma_{fY}h + \sigma_{lY}c. \qquad (56)$$

For simplicity we assume that the plastic membrane force N_o due to the core is unaffected by the degree of core compression; while this assumption is thought to be reasonable for all the cores considered, it requires experimental verification. We now introduce the nondimensional geometric variables of the sandwich beam

$$\bar{c} \equiv \frac{c}{L}, \quad \bar{h} \equiv \frac{h}{c}, \quad \hat{c} \equiv \bar{c}(1 - \epsilon_c), \quad \text{and} \quad \hat{h} \equiv \frac{\bar{h}}{1 - \epsilon_c}, \qquad (57)$$

and the nondimensional core properties

$$\bar{\rho} \equiv \frac{\rho_c}{\rho_f}, \quad \bar{\sigma}_l \equiv \frac{\sigma_{lY}}{\sigma_{fY}} \quad \text{and} \quad \bar{\sigma}_n \equiv \frac{\sigma_{nY}}{\sigma_{fY}}. \qquad (58)$$

The nondimensional structural response time $\bar{T}$ and blast impulse $\bar{I}$ are

$$\bar{T} \equiv \frac{T}{L}\sqrt{\frac{\sigma_{fY}}{\rho_f}}, \quad \bar{I} \equiv \frac{I}{L\sqrt{\rho_f \sigma_{fY}}} \equiv \frac{\hat{I}\bar{c}\sqrt{\bar{\sigma}_n \epsilon_D \bar{h}}}{\zeta}, \qquad (59)$$

where ζI is the blast impulse transmitted to the structure by the fluid. Consequently, the response time T, as given by (53), can be rewritten in the nondimensional form as

$$\bar{T} = \frac{\alpha_2}{2}\frac{\bar{c}(2\bar{h} + \bar{\rho})}{\bar{I}\zeta}\left[\sqrt{1 + \frac{4\bar{I}^2\zeta^2\alpha_3}{3\alpha_1\alpha_2}} - 1\right]$$

$$+ \sqrt{\frac{\bar{c}(2\bar{h} + \bar{\rho})}{3\hat{c}(2\hat{h} + \bar{\sigma}_l\bar{c}/\hat{c})}}\tan^{-1}\left[4\bar{I}\zeta\sqrt{\frac{\alpha_3}{3\alpha_1\alpha_2 + 4\bar{I}^2\zeta^2\alpha_3}}\right], \qquad (60)$$

where

$$\alpha_1 = \hat{c}^3[(1 + 2\hat{h})^2 - 1 + \bar{\sigma}_l\bar{c}/\hat{c}](1 + 2\hat{h})\bar{c}(\bar{\rho} + 2\bar{h}), \qquad (61a)$$

$$\alpha_2 = \frac{\hat{c}[(1 + 2\hat{h})^2 - 1 + \bar{\sigma}_l\bar{c}/\hat{c}]}{2\hat{h} + \bar{\sigma}_l\bar{c}/\hat{c}}, \quad \text{and} \qquad (61b)$$

$$\alpha_3 = \hat{c}(1 + 2\hat{h}). \qquad (61c)$$

The maximum defection (54) of the inner and outer faces at the midspan can be written nondimensionally as

$$\bar{w} \equiv \frac{w}{L} = \frac{\alpha_2}{2}\left[\sqrt{1 + \frac{8\bar{I}^2\zeta^2\alpha_3}{3\alpha_1\alpha_2}} - 1\right], \qquad (62a)$$

and

$$\bar{w}_o = \bar{w} + \epsilon_c\bar{c}, \qquad (62b)$$

respectively. It is emphasized that the deflection of the inner face of the sandwich beam is due to only stage III of the deformation history, while the deflection of the outer face is the sum of the deflections in stage III and the deflection due to core compression in stage II.

It is difficult to give a precise failure criterion for the beam as it is anticipated that the blast impulse for incipient failure is sensitive to the details of the built-in end conditions of the clamped beams. Here, we state a failure criterion based on an estimate of the tensile strain in the face sheets due to stretching of the beam and neglect the tensile strains due to bending at the plastic hinges. The tensile strain ϵ_m in the face sheets due to stretching is approximately equal to

$$\epsilon_m = \frac{1}{2}\left(\frac{w}{L}\right)^2. \qquad (63)$$

By setting this strain ϵ_m to equal the tensile ductility ϵ_f of the face sheet material, an expression is obtained for the maximum nondimensional impulse $\bar{I}_c$ that the sandwich beam can sustain without tensile failure of the face sheets; substitution of (63) into (62a), with the choice $\epsilon_m = \epsilon_f$, gives

$$\bar{I}_c = \frac{1}{\zeta}\sqrt{\frac{3\alpha_1\alpha_2}{8\alpha_3}\left[\left(\frac{2\sqrt{2\epsilon_f}}{\alpha_2} + 1\right)^2 - 1\right]}. \qquad (64)$$

The above analysis, comprising stages I, II, and III for the response of a clamped sandwich beam to blast loading, gives the deflection $\bar{w}$, response time $\bar{T}$, the core compression ϵ_c and the maximum tensile strain ϵ_m in the sandwich beam in terms of

i. the loading parameters as specified by the blast impulse $\bar{I}$, and the fluid-structure interaction parameter ψ,
ii. the beam geometry $\bar{c}$ and $\bar{h}$, and
iii. the core properties as given by the core relative density $\bar{\rho}$, its longitudinal tensile strength $\bar{\sigma}_l$, compressive strength $\bar{\sigma}_n$ and its densification strain ϵ_D.

We proceed to illustrate graphically the functional dependence of $\bar{w}$, $\bar{T}$, ϵ_c, and ϵ_m on the blast impulse $\bar{I}$. Consider a represen-

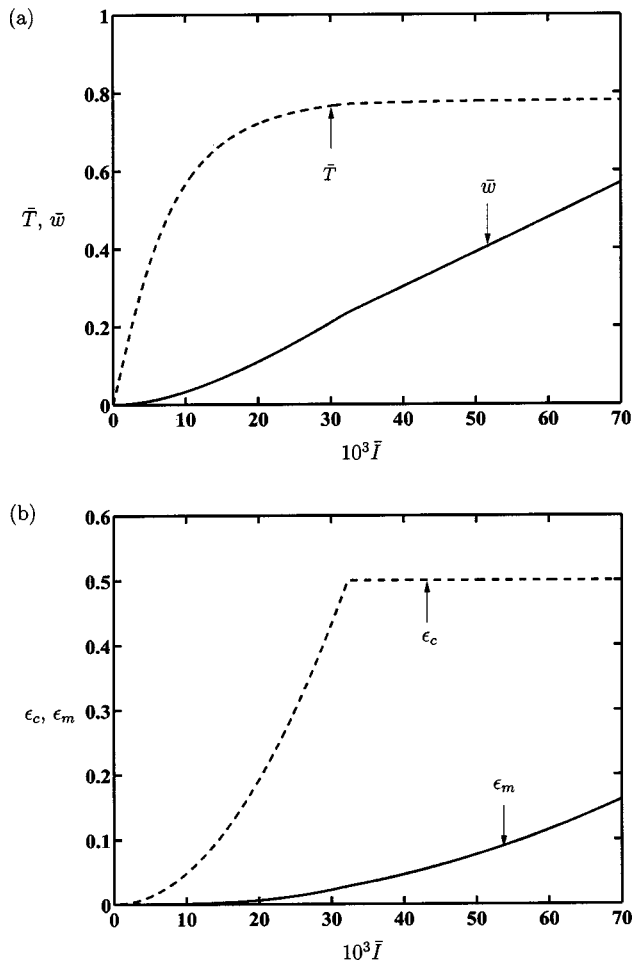**Fig. 6 Response of a clamped sandwich beam ($\bar{c}=0.1,\bar{h}=0.1$) with a pyramidal core ($\bar{\rho}=0.1,\epsilon_Y=0.002,\epsilon_D=0.5$) for an assumed $\psi=1.78$; (a) the normalized response time $\bar{T}$ and deflection $\bar{w}$ and (b) core compression ϵ_c, and tensile strain in beam ϵ_m, as a function of the normalized blast impulse $\bar{I}$**

tative sandwich beam with $\bar{c}=\bar{h}=0.1$ and comprising a pyramidal core of relative density $\bar{\rho}=0.1$ made from the same solid material as the face sheets (with $\epsilon_Y=0.2\%$). As specified in Section II, the core yields rather than elastically buckles, and the normal and longitudinal strengths of this pyramidal core are $\bar{\sigma}_n=0.05$ and $\bar{\sigma}_l=0$, respectively. The densification strain of the core is taken as $\epsilon_D=0.5$. To complete the specification, we assume a fluid-structure interaction parameter $\psi=1.79$ which is representative of an underwater blast with a time constant $\theta=0.1$ ms and 10 mm thick steel faces as discussed in Section III A. The normalized deflection $\bar{w}$ of the inner face of the sandwich beam and response time $\bar{T}$ are plotted in Fig. 6(a) as a function of the normalized blast impulse while the compression ϵ_c and tensile stretch ϵ_m are plotted in Fig. 6(b). For $\bar{I}<0.03$, the compressive strain ϵ_c induced in the core in Stage II is less than ϵ_D and $\bar{w}$ increases approximately quadratically with $\bar{I}$. At higher impulses the core compression is fixed at the densification limit ϵ_D and $\bar{w}$ scales approximately linearly with $\bar{I}$. On the other hand, the structural response time initially increases linearly with $\bar{I}$, but at high impulses the beam behaves as a stretched plastic string and $\bar{T}$ is almost independent of the magnitude of $\bar{I}$.

4 Performance Charts for Water Blast Resistance

The analysis detailed above is now used to investigate the relative response of monolithic and sandwich beams to blast loading.

In a typical design scenario, the solid material and length of the structural element are dictated by design constraints such as corrosion resistance and bulkhead spacing, thus leaving the sandwich panel geometry, viz. the face sheet and core thickness, and core relative density and topology, as the free design variables. Two design problems will be addressed:

1. For a given material combination, beam length and blast impulse, what is the relation between sandwich geometry and the inner face sheet deflection?
2. For a given material combination, beam length and allowable inner face sheet deflection, what is the relation between the required sandwich geometry and the level of blast impulse?

4.1 Monolithic Beams. As a reference case we first present the response of a monolithic beam subjected to a water blast. Consider a monolithic beam of thickness h and length $2L$ made from a rigid-ideally plastic solid material of density ρ_f and yield strength σ_{fY} subjected to a blast impulse I.

We define a fluid-structure interaction parameter $\bar{\psi}$

$$\bar{\psi}=\psi\frac{h}{L}=\frac{\rho_w c_w \theta}{\rho_f L}, \tag{65}$$

which is closely related to the Taylor [1] fluid-structure interaction parameter ψ but written in terms of the specified beam length. The impulse I_{trans} transmitted to the beam is given by (20b) for a specified value of $\bar{\psi}$ and a known beam geometry h/L.

First, we specialize the analysis of Section 3.4 to the case of a monolithic beam with plastic moment $M_o=N_o h/4$, where $N_o=h\sigma_{fY}$ is the plastic membrane force. The nondimensional maximum deflection of the midspan of the beam $\bar{w}=w/L$ and normalized structural response time $\bar{T}\equiv T/L\sqrt{\rho_f/\sigma_{fY}}$ follow from (54) and (53), respectively, as

$$\bar{w}=\frac{h}{2L}\left[\sqrt{1+\frac{8\bar{I}^2\zeta^2}{3}\left(\frac{L}{h}\right)^4}-1\right] \quad \text{and} \tag{66a}$$

$$\bar{T}=\frac{1}{2\bar{I}\zeta}\left(\frac{h}{L}\right)^2\left[\sqrt{1+\frac{4}{3}\bar{I}^2\zeta^2\left(\frac{L}{h}\right)^4}-1\right]$$

$$+\frac{1}{\sqrt{3}}\tan^{-1}\left[\frac{2\bar{I}\zeta(L/h)^2}{\sqrt{3+4\bar{I}^2\zeta^2(L/h)^4}}\right], \tag{66b}$$

where ζI is the impulse transmitted into the structure. For $\zeta\bar{I}\ll 1$, the above relations reduce to

$$\bar{w}=\frac{2}{3}\bar{I}^2\zeta^2\left(\frac{L}{h}\right)^3 \tag{67}$$

$$\bar{T}=\bar{I}\zeta\left(\frac{L}{h}\right)^2, \tag{68}$$

which are identical to the small deflection predictions of Symonds [11].

With the tensile strain in the beam given by (63), the maximum impulse $\bar{I}_c$ sustained by a monolithic beam made from material of tensile ductility ϵ_f is

$$\bar{I}_c=\frac{1}{\zeta}\sqrt{\frac{3}{8}\left(\frac{h}{L}\right)^2\left[\left(2\sqrt{2\epsilon_f}\left(\frac{L}{h}\right)+1\right)^2-1\right]}. \tag{69}$$

A representative design chart is now constructed for a monolithic beam subjected to a water blast. Consider a steel beam of length $2L=10$ m subjected to a blast with a decay time $\theta=0.12$ ms. The
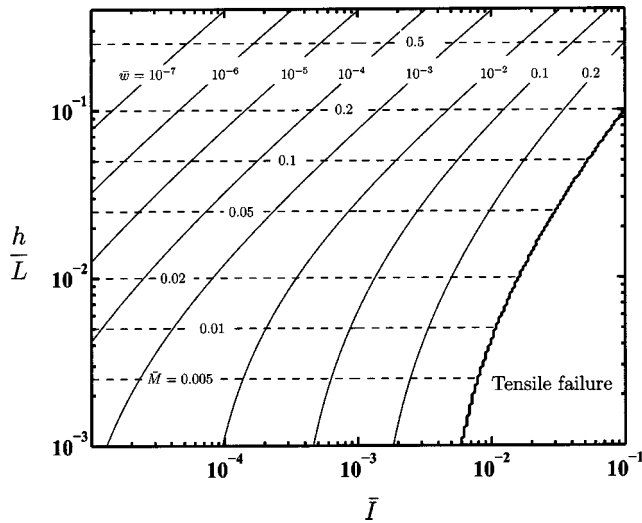
Fig. 7 Design chart for a monolithic beam of tensile ductility $\epsilon_f = 0.2$, subjected to a water blast with $\bar{\psi} = 5 \times 10^{-3}$. Contours of the midspan displacement $\bar{w}$ are given as solid lines and contours of dimensionless mass $\bar{M}$ are shown as dotted lines.

Fig. 8 Design chart for a sandwich beam, with a pyramidal core ($\bar{\rho} = 0.1, \epsilon_Y = 0.002, \epsilon_D = 0.5$), subjected to a water blast. The nondimensional impulse is $\bar{I} = 10^{-2}$, and the fluid-structure interaction parameter is taken as $\bar{\psi} = 5 \times 10^{-3}$. The regime of tensile failure is shown for an assumed tensile ductility of face sheets of $\epsilon_f = 0.2$. Contours of $\bar{w}$ and ϵ_c are included.

fluid-structure interaction parameter $\bar{\psi}$ then takes the value $\bar{\psi} = 5 \times 10^{-3}$. Contours of nondimensional deflection $\bar{w}$ are plotted in Fig. 7 as a function of the normalized blast impulse $\bar{I}$ and beam geometry, h/L, for $\bar{\psi} = 5 \times 10^{-3}$. Note that the contours of the $\bar{w}$ have been truncated at high impulses due to tensile tearing as dictated by (69), with the choice $\epsilon_f = 0.2$. Contours of nondimensional mass $\bar{M} = M/(L^2 \rho_f) = 2h/L$, where M is the mass per unit width of the beam, have also been added to the figure. As expected, the beam deflection increases increasing with blast impulse, for a beam of given mass.

4.2 Sandwich Beams. The blast response of clamped sandwich beams, comprising solid faces and the five types of cores discussed in Section 2, will be analyzed in this section. We restrict attention to cores made from the same solid material as the solid face sheets in order to reduce the number of independent nondimensional groups by one. With the sandwich beam length and material combination specified, the design variables in the problem are the nondimensional core thickness $\bar{c} \equiv c/L$ and face sheet thickness $\bar{h} \equiv h/c$.

Figure 8 shows a design chart with axes $\bar{c}$ and $\bar{h}$ for a clamped sandwich beam with a pyramidal core ($\bar{\rho} = 0.1$, $\epsilon_Y = 0.002$) and subjected to a normalized blast impulse $\bar{I} = 10^{-2}$. The fluid-structure interaction parameter is again taken as $\bar{\psi} = 5 \times 10^{-3}$; this is representative for steel sandwich beams of length $2L = 10$ m subject to a water blast with a decay constant $\theta = 0.12$ ms. Further, the densification strain ϵ_D of the core is assumed to be 0.5 and the tensile ductility of the solid steel is taken as $\epsilon_f = 0.2$. Contours of nondimensional maximum deflection of the mid-span of the inner face of the beam and contours of the compressive strain ϵ_c in the core have been added to the chart: both $\bar{w}$ and ϵ_c increase with decreasing $\bar{c}$ and beam failure by tensile tearing of the face sheets is evident at the top left-hand corner of the chart.

The effect of the fluid-structure interaction parameter $\bar{\psi}$ upon the likelihood of tensile failure of the above sandwich beam is shown in Fig. 9. The figure shows the regime of tensile failure of the face sheets on a design chart with axes $(\bar{c}, \bar{h})$. Apart from the choice of $\bar{\psi}$, the nondimensional parameters are the same as those used to construct Fig. 8: $\bar{\rho} = 0.1$ and $\epsilon_D = 0.5$ for the pyramidal core, $\epsilon_f = 0.2$ for the faces and $\bar{I} = 10^{-2}$. With increasing values of
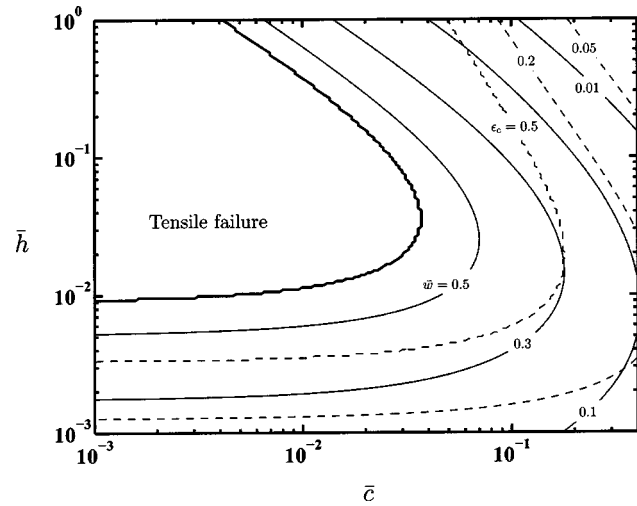
$\bar{\psi}$ (associated with shorter spans, $2L$, and with longer values of the decay constant θ), tensile failure is less likely. Thus, tensile failure is unlikely to occur for sandwich beams provided $\bar{\psi}$ exceeds approximately 0.02.

The inverse design problem of the relation between the pyramidal core ($\bar{\rho} = 0.1$, $\epsilon_Y = 0.002$, $\epsilon_D = 0.5$) sandwich beam geometry and the blast impulse for a specified deflection $\bar{w} = 0.1$ and for $\bar{\psi} = 5 \times 10^{-3}$ is addressed in Fig. 10. Tensile failure of the steel faces ($\epsilon_f = 0.2$) is inactive for the choice $\bar{w} = 0.1$. For the purposes of selecting sandwich beam geometries that maximise the blast impulse at a given mass subject to the constraint of a maximum allowable inner face deflection $\bar{w}$, contours of non-dimensional mass $\bar{M}$ have been added to Fig. 10, where
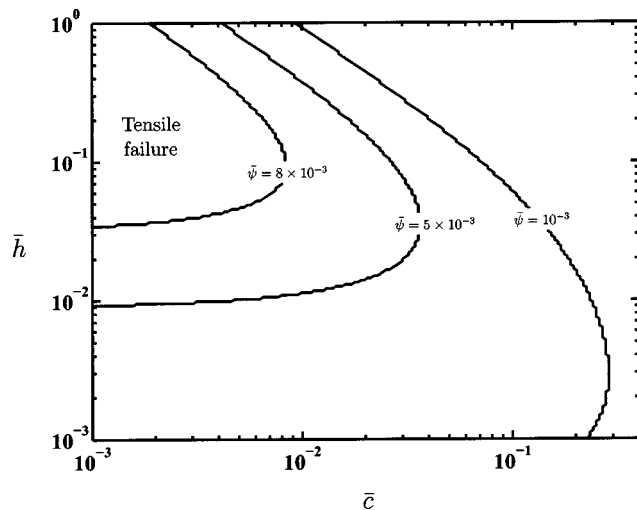

Fig. 9 The effect of $\bar{\psi}$ upon the magnitude of the tensile failure regime within the design chart, for face sheets of ductility $\epsilon_f = 0.2$. The sandwich beam has a pyramidal core ($\bar{\rho} = 0.1, \epsilon_Y = 0.002, \epsilon_D = 0.5$) and the nondimensional impulse is taken as $\bar{I} = 10^{-2}$.
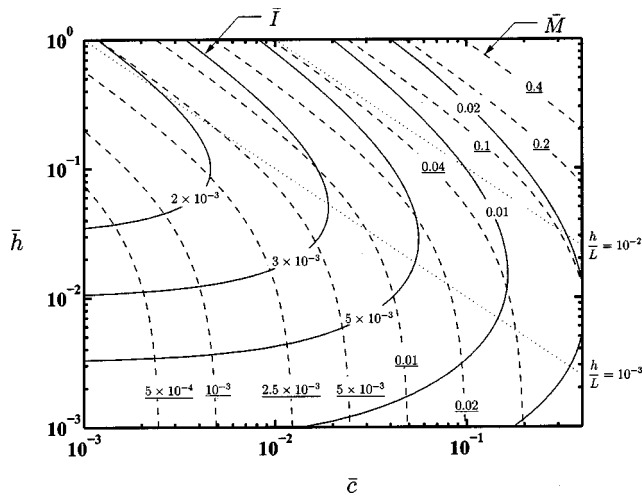
Fig. 10 Design chart for a sandwich beam, with a pyramidal core ($\bar{\rho} = 0.1$, $\epsilon_Y = 0.002$, $\epsilon_D = 0.5$), subjected to a water blast. The beam deflection is $\bar{w} = 0.1$ and the fluid-structure interaction parameter is taken as $\bar{\psi} = 5 \times 10^{-3}$. Contours of $\bar{I}$ and $\bar{M}$ are displayed. The dotted lines trace the paths of selected values of h/L.
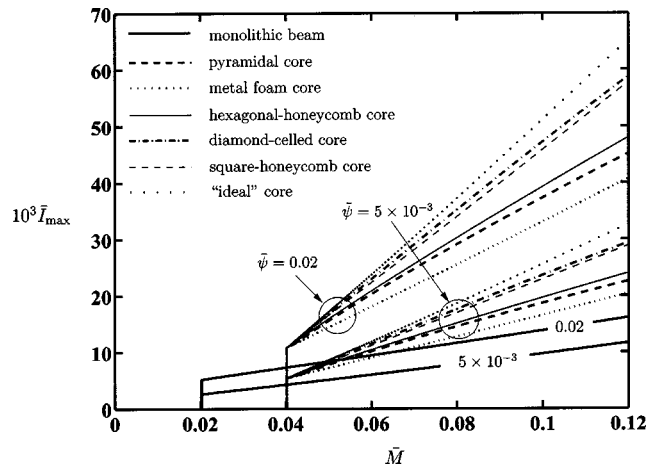

Fig. 11 A comparison of the maximum blast impulse sustained by monolithic beams and by optimal designs of sandwich beams, subjected to the constraints $\bar{w} \leq 0.1$ and $h/L \geq 10^{-2}$. Results are presented for $\bar{\psi} = 5 \times 10^{-3}$ and 0.02. The core relative density is $\bar{\rho} = 0.1$ and densification strain is $\epsilon_D = 0.5$.

$$\bar{M} = \frac{M}{\rho_f L^2} = 2(2\bar{h}\bar{c} + \bar{c}\bar{\rho}), \tag{70}$$

and M is the mass per unit width of the sandwich beam. The figure reveals that geometries that maximize the blast impulse $\bar{I}$ for a given mass $\bar{M}$ have $\bar{h} \to 0$ at almost constant $\bar{c}$, implying that $h/L \to 0$. The physical interpretation is as follows. With decreasing face sheet thickness (or face sheet mass) the blast impulse transmitted to the structure reduces: The Taylor analysis gives $\bar{I}_{\mathrm{trans}} \to 0$ as $h \to 0$. This limit is practically unrealistic as a minimum face sheet thickness is required for other reasons, for example to withstand wave loading, quasi-static indentation by foreign objects such as rocks and other vessels and fragment capture in a blast event. Consequently, we add the additional constraint of a minimum normalized face sheet thickness h/L into the analysis. Contours of h/L for two selected values of h/L have been added to Fig. 10. These lines represent limits on acceptable sandwich beam designs, with designs lying above these lines satisfying the constraint on h/L: designs that maximize blast impulse for a given mass then lie along the lines of constant h/L.

The maximum blast impulse sustained by the sandwich beams with the five different topologies of the core (but $\bar{\rho} = 0.1$, $\epsilon_Y = 0.002$ and $\epsilon_D = 0.5$ in all cases), subject to the constraints $h/L > 10^{-2}$ and the inner face deflection $\bar{w} \leq 0.1$ are plotted in Fig. 11 as a function of the nondimensional mass $\bar{M}$ for the choice $\bar{\psi} = 5 \times 10^{-3}$. For comparison purposes, the blast impulse sustained by a monolithic beam subjected to the same constraints is also included in Fig. 11. It is evident that sandwich beams all perform considerably better than the monolithic beam. This is mainly due to the fact that the sandwich beams have a thin outer face sheet which results in a small impulse transmitted into the structure whereas the relatively thick beams in monolithic design absorb a larger fraction of the blast impulse. A comparison of the various sandwich cores shows that sandwich beams with a metal foam and pyramidal core almost attain the performance of the hexagonal-honeycomb core. However, the diamond-celled and square-honeycomb core beams, which have high strength in both the through-thickness and longitudinal directions, out perform the other sandwich beams. The performance of the diamond-celled core beam approaches that of the "ideal" sandwich core. It is noted that $\bar{M}$ has minimum achievable values. This is explained as follows. Since $h/L \equiv \bar{h}\bar{c}$, the expression (70) for $\bar{M}$ can be rewritten as

$$\bar{M} = 4\frac{h}{L} + 2\bar{c}\bar{\rho}. \tag{71}$$

The above constraint on the minimum h/L implies a minimum value for $\bar{M}$ of $4h/L$. Thus, for the constraint $h/L \geq 10^{-2}$, $\bar{M}$ has the minimum value of 0.04 as evident in Fig. 11. Similarly, for a monolithic beam of thickness h, $\bar{M}$ is given by $\bar{M} = 2h/L$ and so a constraint on the minimum value of h/L gives directly a minimum acceptable mass $\bar{M}$. With increasing values of the $\bar{\psi}$, the fraction of the blast impulse transmitted into the structure decreases and thus all the beams sustain higher blast. However, the relative performance of the various beam configurations remains unchanged.

The effect of the constraint on h/L on the performance of the above sandwich beams is illustrated in Fig. 12 for the choice $\bar{\psi} = 5 \times 10^{-3}$. As the allowable minimum value of h/L decreases from 10^{-2} to 10^{-3}, the blast impulses sustained by the sandwich beams increase. Further, the rankings of the cores change slightly: while the diamond-celled core still performs the best followed by the square-honeycomb core, the metal foam core is now seen to out perform the pyramidal and hexagonal-honeycomb cores at higher masses. This can be rationalized as follows. Upon imposing the constraint $h/L \geq 10^{-3}$, a large fraction of the mass of the sandwich beam is in the core. Recall that the pyramidal and hexagonal-honeycomb cores have no longitudinal strength while the metal foam core gives some additional longitudinal stretching resistance to the sandwich beam, and this results in its superior performance.

So far we have determined the optimal designs of sandwich beams for a midspan deflection of $\bar{w} \leq 0.1$. But how does the relative performance depend upon the allowable value of $\bar{w}$? The performance of the sandwich beams with constraints $h/L \geq 10^{-2}$ and $\bar{\psi} = 5 \times 10^{-3}$ is illustrated in Fig. 13 for $\bar{w} \leq 0.1$ and $\bar{w} \leq 0.4$. As expected, the beams can sustain higher impulses when the constraint on $\bar{w}$ is relaxed to $\bar{w} \leq 0.4$. However, the rankings change for the two levels of $\bar{w}$ considered in Fig. 13. With the higher allowable deflections, the longitudinal stretching of the core becomes increasingly important and the metal foam core out performs the pyramidal or hexagonal-honeycomb cores. The
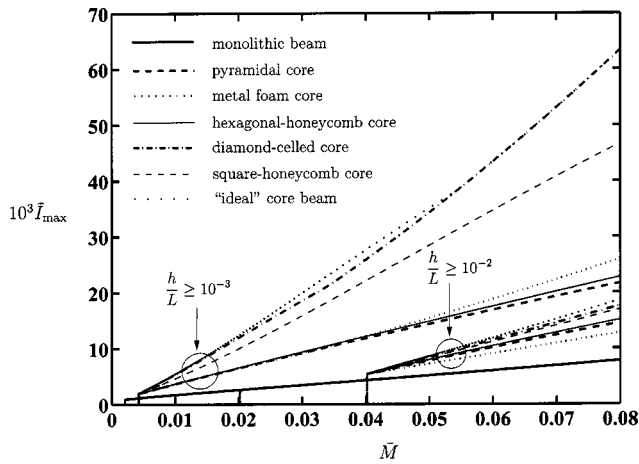
Fig. 12 A comparison of the maximum blast impulse sustained by monolithic beams and by optimal designs of sandwich beams, subjected to the constraint $\bar{w} \leq 0.1$ with $\bar{\psi} = 5 \times 10^{-3}$. Results are presented for constraints $h/L \geq 10^{-2}$ and 10^{-3}. The core relative density is $\bar{\rho} = 0.1$, $\epsilon_Y = 0.002$ and densification strain is $\epsilon_D = 0.5$.

diamond-celled core has a high compressive and an ideal longitudinal strength, and has a blast performance which is nearly indistinguishable from that of the "ideal" core under the constraint $\bar{w} \leq 0.4$.

In the above analysis the relative density of the core has been taken to be $\bar{\rho} = 0.1$, and the yield strain of the core material taken to be representative of that for structural steels, $\epsilon_Y = 0.002$. Consequently, the individual struts of the pyramidal and diamond-celled cores deform by plastic yield. We proceed to investigate the blast performance of the pyramidal and diamond-celled core sandwich beams at relative densities $\bar{\rho}$ such that elastic buckling of the core members can intervene. The optimal performance of diamond-celled core sandwich beams with the constraints $h/L \geq 10^{-2}$ and $\bar{w} \leq 0.1$ is plotted in Fig. 14(a) for selected values of core relative density $\bar{\rho} = 0.02$, 0.05, 0.1 and 0.2. The core is assumed to be made from a solid of yield strain $\epsilon_Y = 0.002$ and consequently cores of density $\bar{\rho} = 0.02$ and 0.05 deform by elastic buckling. While the performance of the low core density beams is
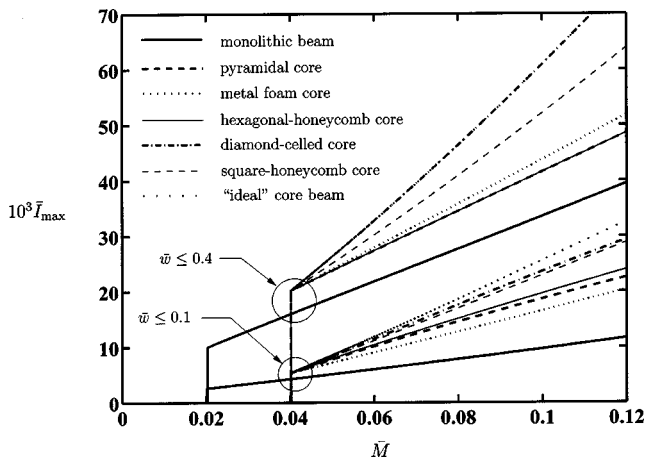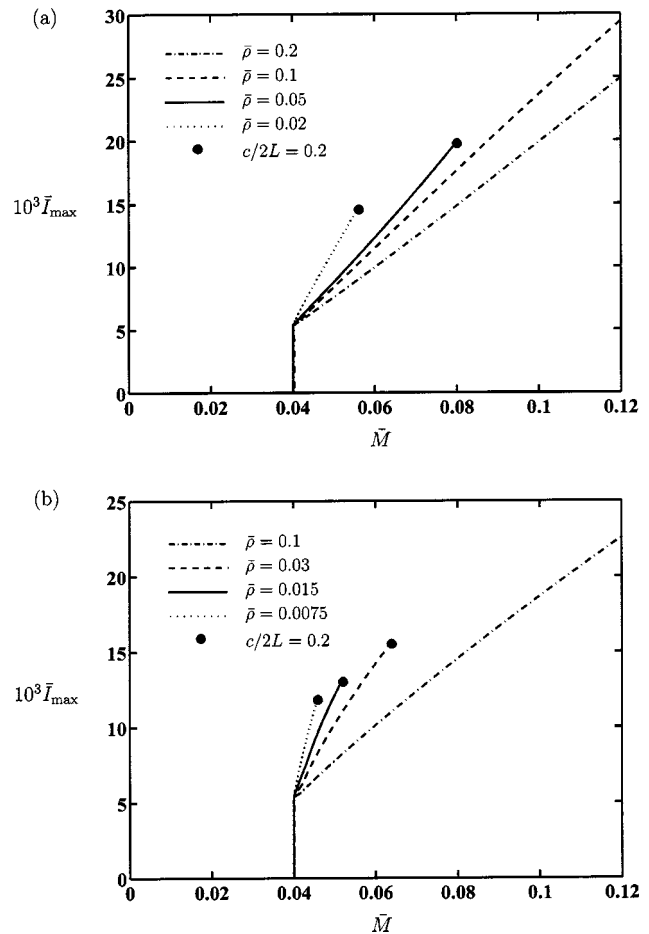

Fig. 14 Comparison of the maximum blast impulse sustained by optimal (a) diamond-celled and (b) pyramidal core sandwich beams for selected core densities, with $\bar{\psi} = 5 \times 10^{-3}$ and $h/L \geq 10^{-2}$, $\bar{w} \leq 0.1$. The yield strain of the core parent material is assumed to be $\epsilon_Y = 0.002$ and densification strain of the core is taken as $\epsilon_D = 0.5$.

slightly superior to the $\bar{\rho} = 0.1$ beams, these beams of low core density have stubby designs with high values of $c/2L$. Thus, these optimal designs become impractical for high blast impulses and the curves in Fig. 14(a) have been truncated at $c/2L = 0.2$. A similar analysis was performed for the pyramidal core; these cores deform by elastic buckling at $\bar{\rho} \leq 0.015$. The results for the optimal blast performance of these beams are summarized in Fig. 14(b); again the low density cores provide superior performance but the beams are stubby (high $c/2L$) and hence practical designs of these beams are unable to sustain high blast impulses. A comparison of Figs. 14(a) and 14(b) reveals that over the entire range of relative densities investigated, the diamond-celled core beams always out perform the pyramidal core beams.

Fig. 13 A comparison of the maximum blast impulse sustained by monolithic beams and by optimal designs of sandwich beams, subjected to the constraint $h/L \geq 10^{-2}$ with $\bar{\psi} = 5 \times 10^{-3}$. Results are presented for constraints $\bar{w} \leq 0.1$ and 0.4. The core relative density is $\bar{\rho} = 0.1$, $\epsilon_Y = 0.002$ and densification strain is $\epsilon_D = 0.5$.

5 A Comparison of Structural Performance Under Air and Water Blast Loading

Due to the low acoustic impedance of air, the Taylor fluid-structure interaction parameter $\psi \approx 0$ for an air blast, as discussed in Section 3.2. In this section we discuss blast loading in air by assuming $\bar{\psi} \equiv \psi h/L = 0$: The entire blast impulse is transmitted to the sandwich structure.
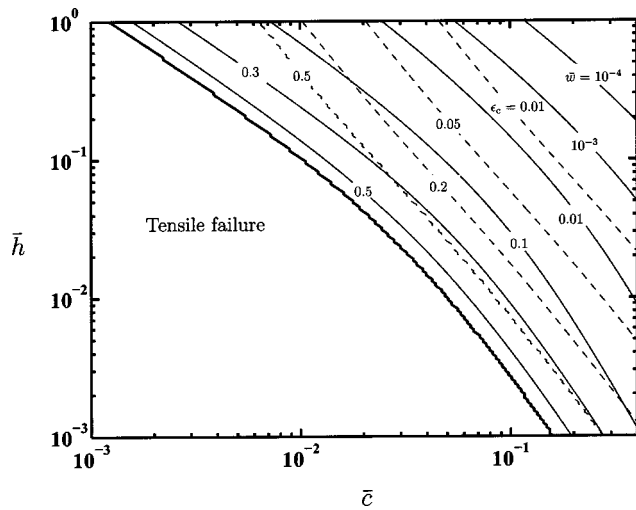
Fig. 15 Design chart for a sandwich beam, with a pyramidal core ($\bar{\rho}=0.1, \epsilon_Y=0.002, \epsilon_D=0.5$), subjected to an air blast. The nondimensional impulse is $\bar{I}=10^{-3}$. The regime of tensile failure is shown for an assumed tensile ductility of face sheets of $\epsilon_f=0.2$. Contours of $\bar{w}$ and ϵ_c are included.

Consider the representative case of a sandwich beam with a pyramidal core ($\bar{\rho}=0.1, \epsilon_D=0.5, \epsilon_Y=0.002$), subjected to an air blast of magnitude $\bar{I}=10^{-3}$. The design chart is given in Fig. 15, with axes of $\bar{c}$ and $\bar{h}$, and with contours displayed for the midspan deflection $\bar{w}$ of the inner face and through-thickness core compression ϵ_c. The tensile ductility of the face sheet material is taken to be $\epsilon_f=0.2$ representative of structural steels; despite this moderately high value of ϵ_f, tensile failure of the face sheets dominates the chart with less than half the design space of Fig. 15 resulting in acceptable designs. In contrast, for water blast (Fig. 8), tensile failure is of less concern even for a higher blast impulse of $\bar{I}=10^{-2}$; the underlying explanation is that only a small fraction of the impulse is transmitted into the sandwich structure for water blast loading.
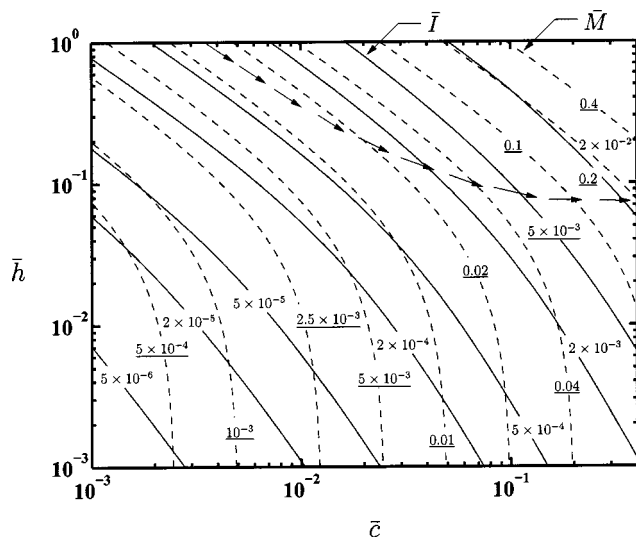

Fig. 17 (a) Comparison of the maximum impulse sustained by monolithic and sandwich beams for an air blast with the constraint $\bar{w} \leqslant 0.1$. The core relative density and densification strain are, $\bar{\rho}=0.1$ and $\epsilon_D=0.5$, respectively, and $\epsilon_Y=0.002$. (b) The optimal designs of sandwich beams with pyramidal and diamond-celled core.

A design map for air blast loading of the above pyramidal core sandwich beam is given in Fig. 16, with contours of $\bar{I}$ required to produce a mid-span deflection of $\bar{w}=0.1$. The figure should be contrasted with the water blast map shown in Fig. 10, again for $\bar{w}=0.1$; the only difference in the assumed values of the plots is that $\bar{\psi}=0$ in Fig. 16 and $\bar{\psi}=5 \times 10^{-3}$ in Fig. 10. While the contours of $\bar{M}$ are identical in the two figures, the contours of $\bar{I}$ are of markedly different shape. For the case of air blast (Fig. 16) there is no need to impose a constraint on the minimum value for h/L: The trajectory of $(\bar{c}, \bar{h})$ which maximizes $\bar{I}$ for a given $\bar{M}$ no longer lies along a line of constant h/L and is associated with $h/L \equiv \bar{h}\bar{c}$ values in the range 0.003 to 0.032. The arrows shown in Fig. 16 trace the optimum designs with increasing mass. This can be contrasted with the water blast problem where the optimum designs lay along the specified minimum value of h/L.

The air blast performance of the optimized sandwich beams is compared to that of the monolithic beam in Fig. 17(a). Specifically, the maximum sustainable impulse is plotted against the nondimensional mass $\bar{M}$, with the deflection constraint $\bar{w} \leqslant 0.1$ imposed. In contrast to the case of water blast, the performance gain upon employing sandwich construction instead of monolithic beams is relatively small; at best the diamond-celled core sustains

Fig. 16 Design chart for a sandwich beam, with a pyramidal core ($\bar{\rho}=0.1, \epsilon_Y=0.002, \epsilon_D=0.5$), subjected to an air blast. The beam deflection is $\bar{w}=0.1$. Contours of $\bar{I}$ and $\bar{M}$ are displayed. The arrows trace the path of designs which maximize the impulsive resistance with increasing mass.
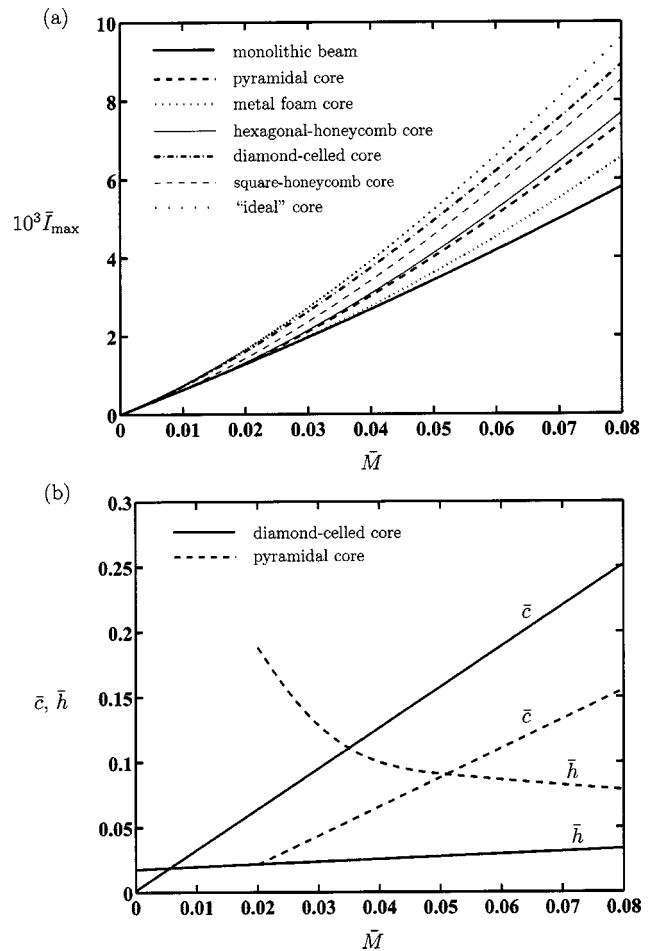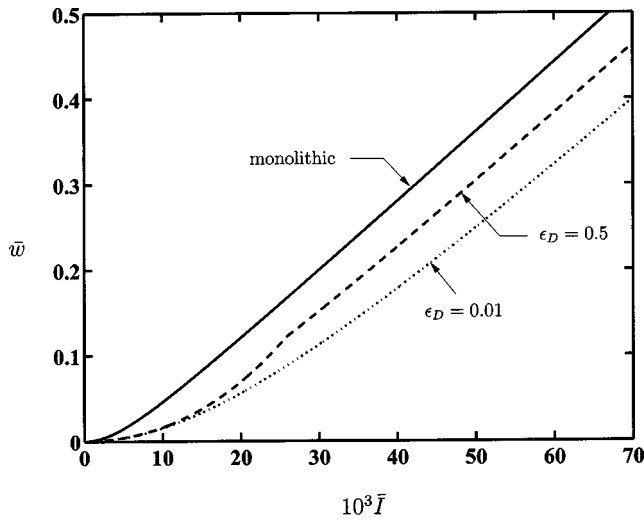
Fig. 18 The normalized deflection of the bottom face of a diamond-celled core ($\bar{\rho}=0.1, \epsilon_Y=0.002$) sandwich beam with $\bar{c} = \bar{h}=0.2$ as a function of the normalized impulse, for two selected values of the core densification strain ϵ_D. The response of a monolithic beam of the same mass $\bar{M}=0.2$ is included.
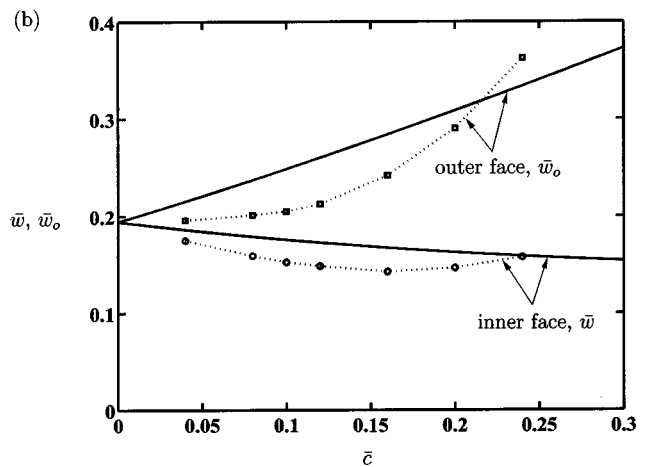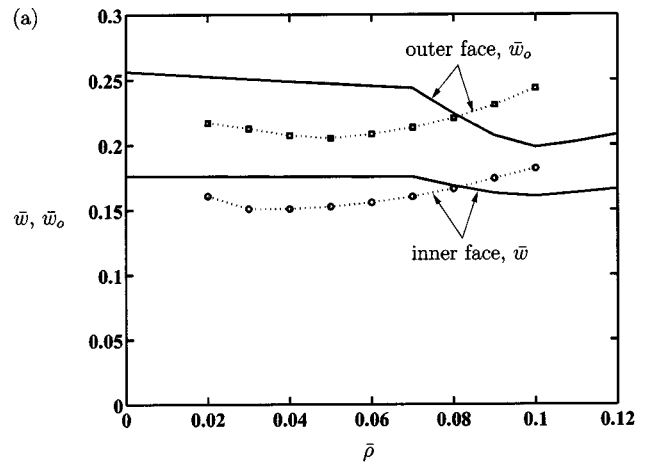

Fig. 19 Comparison of the analytical predictions and the three-dimensional FE predictions of Xue and Hutchinson [6] for the deflection of sandwich beams with a corrugated core. The beams have a mass $\bar{M}=0.04$ and are subjected to an impulse $\bar{I}=5\times10^{-3}$. The effect upon $\bar{w}$ and $\bar{w}_o$ of (a) core relative density $\bar{\rho}$ for $\bar{c}=0.1$ and (b) $\bar{c}$ with the core relative density held fixed at $\bar{\rho}=0.04$. The solid lines give the analytic solutions and the dotted lines (with symbols) give the FE results.

an impulse about 45% greater than a monolithic beam of equal mass. The geometry of the optimal pyramidal and diamond-celled sandwich core beams of Fig. 17(a) are plotted in Fig. 17(b). For both configurations, $\bar{c}$ increases with increasing mass, with the optimal pyramidal core beams having a lower $\bar{c}$ (and a higher $\bar{h}$) as compared to the optimal diamond-celled core beams.

In water blast, the sandwich beam out performs the monolithic beam mainly due to the fact that the thin (and therefore light) outer face of the sandwich beam acquires a smaller fraction of the blast impulse compared to the relatively thick monolithic beam. However, in the case of air blast, the full blast impulse is transmitted to the structure for both the sandwich and monolithic beams. The superior air blast resistance of sandwich beams to monolithic beams, as seen in Fig. 17(a) is attributed solely to the shape factor effect of the sandwich construction. To clarify this point, the deflection of a sandwich beam with a diamond-celled core ($\bar{\rho}=0.1, \bar{c}=\bar{h}=0.2$) is plotted in Fig. 18 as a function of the air impulse for two assumed values of core densification strain $\epsilon_D=0.01$ and $\epsilon_D=0.5$ along with the response of a monolithic beam of equal mass $\bar{M}=0.2$. Figure 18 reveals that the beam with the core densification strain $\epsilon_D=0.01$ which maintains the separation of the face sheets and is the strongest while the monolithic beam is the weakest: it is the shape factor effect that gives the sandwich construction structural advantage in air blast.

6 Comparison With Three-Dimensional Finite Element Simulations

Xue and Hutchinson [6] conducted three-dimensional finite element (FE) simulations of the dynamic response of clamped sandwich beams with the corrugated, square-honeycomb, and pyramidal core geometries. In these FE simulations, Xue and Hutchinson [6] modelled the core members explicitly including the development of contact between the core members and the face sheets under increasing through-thickness compressive strain. An impulse was applied to the front face of the sandwich beam and thus their numerical results can be compared directly to our analytical predictions for air blast, with $\bar{\psi}=0$.

Xue and Hutchinson [6] modeled sandwich beams made from 304 stainless steel and assumed an elastic, power-law hardening stress versus strain response for the solid steel with a yield strain $\epsilon_Y=0.2\%$ and a power law hardening exponent $N=0.17$. In the analytic predictions given below we assume a rigid, ideally plastic

solid material response, and include elastic buckling of the core members by assuming a solid material yield strain $\epsilon_Y=0.2\%$. In line with experimental data for metal foams, we take the densification strain ϵ_D of the core to be related to the relative density $\bar{\rho}$ through, [2],

$$\epsilon_D=0.8-1.75\bar{\rho}. \qquad (72)$$

Xue and Hutchinson [6] investigated the effects of core relative density and core thickness for sandwich beams of total mass $\bar{M}=0.04$ and considered an impulse $\bar{I}=5\times10^{-3}$. Comparisons between the FE and analytical predictions of the maximum face sheet displacements of the corrugated core sandwich beams are shown in Fig. 19: In Fig. 19(a) the effect of core relative density is investigated with $\bar{c}=0.1$, while in Fig. 19(b) the effect of $\bar{c}$ is studied for a core of relative density $\bar{\rho}=0.04$. While the analytical predictions are within 15% of the FE calculations in all cases, the analytical model does not capture the qualitative form of the variations as predicted by the FE analysis. A careful comparison with the FE results indicates that this is mainly due to the fact that for $\bar{I}=5\times10^{-3}$, the analytical solutions predict full densification
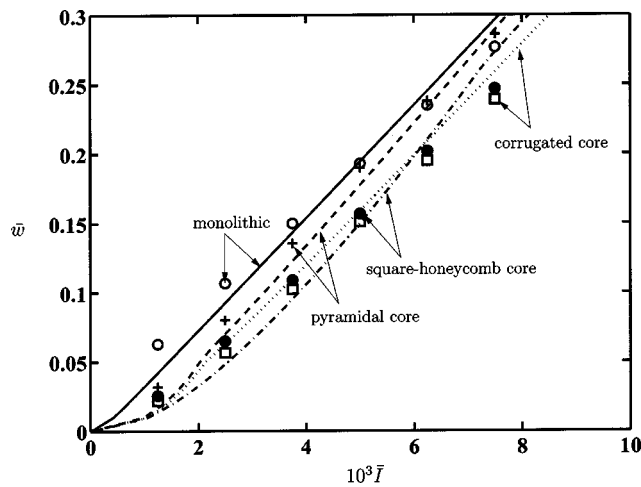
Fig. 20 Comparison of the analytical predictions and the three-dimensional FE predictions of Xue and Hutchinson [6] for the deflection $\bar{w}$ of monolithic beams and sandwich beams with corrugated, square-honeycomb, and pyramidal cores. The beams have a fixed mass $\bar{M}=0.04$ and the sandwich beams have a core of relative density $\bar{\rho}=0.04$ and aspect ratio $\bar{c}=0.1$. The symbols denote the FE results while the lines are the analytical predictions.

in nearly all cases while in the FE simulations no distinct densification limit exits; rather, continued core compression occurs at increasing stress level after contact has begun between the core members and the face sheets. An improved core constitutive model with continued hardening rather than lockup after some critical strain ϵ_D may be able to address this deficiency; this is however beyond the scope of the present study.

Xue and Hutchinson [6] employed a series of FE calculations to identify a "near-optimal" sandwich configurations with mass $\bar{M}=0.04$. They concluded that a sandwich beam with a core of relative density $\bar{\rho}=0.04$ and $\bar{c}=0.1$ (giving $\bar{h}=0.08$) is an optimal configuration for a moderately large blast. Comparisons between the FE and analytical predictions (with the choice $\epsilon_D=0.5$) of the deflections of the inner face sheet of these "optimum" sandwich beams as a function of blast impulse are shown in Fig. 20. Over the range of impulses considered, the analytical predictions are within 10% of the three-dimensional FE calculations for the pyramidal, corrugated and square-honeycomb core sandwich beams as well as for the monolithic beams. Note that the FE calculations predict that the monolithic beam out performs the pyramidal core sandwich beam (i.e., smaller deflections at the same impulse) for impulses $\bar{I}>5\times10^{-3}$. This is due to the wrinkling of the face sheets between the nodes of the pyramidal truss. While this effect is not included in the current analysis, the analytical model too will predict that the monolithic beam out performs the pyramidal core beam at large deflections: at large deflections the degree of axial stretching becomes significant, yet the pyramidal core provides no longitudinal strength.

7 Discussion

An approximate analytical methodology has been presented to predict the dynamic response of sandwich beams to blast loadings in air and water. A number of approximations have been made to make the problem tractable to an analytical solution. Principally, these are (i) the one-dimensional approximation of the blast event, (ii) separation of the stages of the response into three sequential phases, (iii) neglect of the support reaction during the blast event and during the core compression phases, and (iv) a highly simplified core constitutive model wherein the core is assumed to behave as a ideally plastic locking solid. The effects of strain hardening and rate sensitivity of the solid material has also been

neglected. Despite these approximations, the analysis has been shown to compare well with three-dimensional FE calculations. Thus, the analysis presented here is not only adequate to explore trends and scaling relations but is also expected to suffice to make approximate predictions for the purposes of selecting core topologies and sandwich beam geometries. The nondimensional formulas presented here bring out the stages of the response clearly and hence aid the interpretation of more accurate numerical calculations such as the recent dynamic finite element analysis of Xue and Hutchinson [6].

Two notes of caution on the model presented here must be mentioned. Recent numerical fluid-structure interaction calculations on similar sandwich structures performed by Belytschko[14] indicate that the one-dimensional Taylor analysis underestimates the impulse transmitted into the sandwich structure and thus the performance gains due to sandwich constructions indicated here may be somewhat optimistic. Second, the failure of the face sheets near the supports by dynamic necking have not been addressed here. Additional investigations are required to establish an appropriate failure criterion under dynamic conditions.

8 Concluding Remarks

An analytical methodology has been developed to analyze the dynamic response of metallic sandwich beams subject to both air and water blasts. The response of the sandwich beams is separated into three sequential stages: Stage I is the fluid-structure interaction problem, stage II is the phase of core compression, and in stage III the clamped beam is brought to rest by plastic stretching and bending. The simple analytical formulas presented above are in good agreement with more accurate three-dimensional FE calculations given in a parallel study of Xue and Hutchinson [6].

The analysis has been used to construct performance charts for the response of both monolithic and sandwich beams subject to both air and water borne blasts. For the case of water blast, an order of magnitude improvement in blast resistance is achieved by employing sandwich construction. This is mainly due to fluid-structure interaction: The reduced mass of the sandwich outer face leads to a reduction in the impulse transmitted to the structure from the water. In air, the impedance mismatch between air and the face sheet is comparable to that between air and a monolithic beam; consequently, the use of sandwich construction gives a more moderate gain in blast resistance compared to monolithic construction. For both air and water blast the diamond-celled core sandwich beam gives the best performance due to the longitudinal strength provided by the core. Comparisons of the predictions presented here with three-dimensional coupled fluid-structure numerical calculations and blast experiments need to be performed to validate and extend this analysis.

References

[1] Taylor, G. I., 1963, "The Pressure and Impulse of Submarine Explosion Waves on Plates," *The Scientific Papers of G. I. Taylor, Vol III*, Cambridge Univ. Press, Cambridge, UK pp. 287–303.
[2] Ashby, M. F., Evans, A. G., Fleck, N. A., Gibson, L. J., Hutchinson, J. W., and Wadley, H. N. G., 2000, *Metal Foams: A Design Guide*, Butterworth Heinemann, London.
[3] Deshpande, V. S., and Fleck, N. A., 2001, "Collapse of Truss Core Sandwich Beams in 3-Point Bending," Int. J. Solids Struct., **38**(36–37), pp. 6275–6305.
[4] Sypeck, D. J., and Wadley, H. N. G., 2001, "Multifunctional Microtruss Laminates: Textile Synthesis and Properties," J. Mater. Res., **16**(3), pp. 890–897.

[5] Deshpande, V. S., and Fleck, N. A., 2003, "Energy Absorption of an Egg-Box Material," J. Mech. Phys. Solids, **51**(1), p. 187.

[6] Xue, Z., and Hutchinson, J. W., 2003, "A Comparative Study of Blast-Resistant Metal Sandwich Plates," Int. J. Impact Eng., submitted for publication.

[7] Cole, R. H., 1948, *Underwater Explosions*, Princeton University Press, Princeton, NJ.

[8] Swisdak, M. M., 1978, "Explosion Effects and Properties—Part II: Explosion Effects in Water," Technical Report, Naval Surface Weapons Center, Dahlgren, VA.

[9] Smith, P. D., and Hetherington, J. G., 1994, *Blast and Ballistic Loading of Structures*, Butterworth Heinemann, London.

[10] Qiu, X., Deshpande, V. S., and Fleck, N. A., 2003, "Finite Element Analysis of the Dynamic Response of Clamped Sandwich Beams," Eur. J. Mech. A/Solids, submitted for publication.

[11] Symmonds, P. S., 1954, "Large Plastic Deformations of Beams Under Blast Type Loading," *Proceedings of the Second U.S. National Congress of Applied Mechanics*, pp. 505–515.

[12] Jones, N., 1971, "A Theoretical Study of the Dynamic Plastic Behavior of Beams and Plates With Finite Deflections," Int. J. Solids Struct., **7**, p. 1007.

[13] Jones, N., 1989, *Structural Impact*, Cambridge University Press, Cambridge, UK.

[14] Belytschko, T., 2003, private communication.